



THE UNIVERSITY *of* EDINBURGH  
School of Engineering

BEng Mechanical Engineering Thesis Project

---

**Design and manufacture of C.U.R.I.C.O: an autonomous  
multi-modal unmanned aerial-aquatic vehicle**

---

Author: Martin Starkov

(Supervisor: Dr. Francesco Giorgio-Serchi)

(Second Marker: Dr. David Garcia Cava)

The University of Edinburgh

May 3, 2023

# Personal Statement

This thesis is submitted in partial fulfillment of the requirements for the degree of BEng in Mechanical Engineering. I declare that the report has been composed by myself and that the work therein is my own, except where explicitly stated in the text. The concept behind this project originates from previous work done by a Master's student at the University of Edinburgh, Filippo Pucci. He also conducted his project under the supervision of Dr. Francesco Giorgio-Serchi, however, chose to focus on the theoretical and modeling side of the hybrid aerial-aquatic vehicle instead of the practical side as I have. In that project, Pucci proved the theoretical viability of the water-to-air transition maneuver using fluid dynamics modeling. The aim of my thesis, however, was to prove its viability by developing a working prototype vehicle that could execute this maneuver and go from the theoretical to the practical. This prototype was by far the most ambitious project I have ever undertaken and I have learned a great deal from it. I set about tackling the project with no prior knowledge about drones or other remote-controlled vehicles but dove in head first to research what makes these amazing machines work. I took what I learned and combined it to produce C.U.R.I.C.O, a hybrid aerial-aquatic vehicle capable of unfolding quickly during an aggressive water exit. During the project, I went to the university laboratories a handful of times to handle materials such as carbon fiber which required proper ventilation but mostly worked self-sufficiently otherwise. The project progressed smoothly until the later stages when electrical failures started appearing left and right due to my lack of past knowledge and the time pressure to finish the project. While it would have been nice to finish all capabilities of the vehicle before the thesis submission deadline, I am confident that my supervisor will support my efforts to implement these features after the deadline has passed. He has already allocated a large amount of resources to make this project happen and I feel I owe it to him to see it through until the end.

Signed: *Martin S.*

May 3, 2023

# Summary

## Title

Design and manufacture of C.U.R.I.C.O: an autonomous multi-modal unmanned aerial-aquatic vehicle

## Author

Martin Starkov

## Date

May 3, 2023

## Abstract

This thesis sets out to design, manufacture, and test C.U.R.I.C.O, an autonomous hybrid aerial-aquatic vehicle capable of conducting a rapid aerial-aquatic transition maneuver. While some research has been conducted on the theoretical viability of these types of vehicles, no practical prototypes currently exist. Most vehicles that attempt multi-modal operation do so by sacrificing maneuverability in both mediums. As such, the medium transition is done in a slow manner. There have been papers that discuss the potential benefits of conducting such a maneuver rapidly, namely the possibility of a vertical thrust benefit due to something called the added mass effect. While this research is outside the scope of the work conducted for this thesis, it shows one future potential application of such a prototype vehicle: to measure and test this effect. Having the ability to maneuver rapidly in both mediums has other benefits as well. The prototype sets to prove that aerial-aquatic hybrid vehicles can be constructed for use cases where time is of the essence, such as underwater search and rescue for sinking ships. The full nuanced design of this vehicle is documented for such vehicles to be easier designed and constructed in the future. The thesis also dives into the experimental characterization of the unfolding mechanism designed as part of the aerial transition system. Finally, the experimental results observed at the end of this thesis are generalized to relate the opening time of such an unfolding mechanism to the elastic force present in the system.

# Acknowledgements

I would like to thank the following people for their contributions to this project:

Francesco for giving me the freedom to pursue this project in whichever way I chose and lifting the burden of a limited financial budget off of me. Your encouraging words kept me motivated throughout the entire process from beginning to end. Talking with you has been effortless and I am eternally grateful for your kindness, guidance, and humility. I had a lot of fun with this project and that is mostly thanks to your support.

Jonah for your unmatched engineering judgment and invaluable insight. I appreciate how effortlessly you agreed to help me even when it inconvenienced you. That is the sign of a true friend and I will not forget that! Please call in more favors so we can be even one day!

Nicole for your unwavering love through a busy time. I appreciate you sitting with me and dealing with the struggles that came as part of this project. I could not have asked for a better partner to support me throughout this time.

My parents and brother for supporting me and regularly asking about my progress. Thank you for all the encouraging words and helpful anecdotes and opinions on every challenge I brought you.

David for the helpful feedback you gave on my interim report, I tried to take away the most I could from our chat!

Calum and John for your expertise in the mechanical and composites laboratories and Colin for your tidbits of advice and interest in my progress.

Sensei, mosca, and driftingS13 from the iNAV discord server for helping a total stranger on short notice and doing so in an incredibly encouraging way. You guys helped me finish strong!

Thank you all!

# Contents

<b>Notation</b>	<b>vii</b>
<b>List of Figures</b>	<b>x</b>
<b>List of Tables</b>	<b>xi</b>
<b>1 Introduction</b>	<b>1</b>
1.1 Aims . . . . .	1
1.2 Objectives . . . . .	1
<b>2 Literature Review</b>	<b>2</b>
2.1 Unmanned Aerial Vehicles . . . . .	2
2.1.1 Quadcopter Applications . . . . .	3
2.2 Unmanned Underwater Vehicles . . . . .	3
2.2.1 Autonomous Underwater Vehicle Operating Principles . . . . .	3
2.3 Unmanned Aerial-Aquatic Vehicles . . . . .	4
2.3.1 Current Challenges in Medium Transition . . . . .	4
2.3.2 Current UAAV Prototypes . . . . .	5
<b>3 Design Philosophy</b>	<b>7</b>
3.1 Evaluation Methods . . . . .	7
3.2 Testing Facility . . . . .	9
3.3 Motion Constraints . . . . .	9
3.4 Risks and Mitigation . . . . .	9
<b>4 Design</b>	<b>10</b>
4.1 Aerial Section . . . . .	10
4.1.1 Aerial Motors and Propellers . . . . .	11
4.1.2 Unfolding Mechanism . . . . .	12
4.1.3 Release Mechanism . . . . .	15
4.2 Aquatic Section . . . . .	17
4.2.1 Aquatic Motor and Propeller . . . . .	18
4.2.2 Nose Cone . . . . .	19
4.2.3 Aquatic Seals and Waterproofing . . . . .	20
4.2.4 Stabilization and Tail Fins . . . . .	22
4.3 Electronics . . . . .	22
4.3.1 Battery . . . . .	24
4.4 Wiring . . . . .	25

4.4.1	Flight Computer . . . . .	25
4.4.2	iNAV Firmware . . . . .	26
4.4.3	PID Controller . . . . .	26
4.4.4	Communication Systems . . . . .	27
4.4.5	Signal Transmission . . . . .	27
<b>5</b>	<b>Manufacturing and Assembly</b>	<b>28</b>
5.1	Structural Elements . . . . .	28
5.2	Electronics Assembly . . . . .	29
5.3	Waterproofing Process . . . . .	29
5.4	Final Assembly . . . . .	29
<b>6</b>	<b>Experiments and Results</b>	<b>32</b>
6.1	Unfolding Mechanism Opening Times . . . . .	32
<b>7</b>	<b>Discussion</b>	<b>37</b>
7.1	Experimental Outcomes . . . . .	37
7.1.1	Sources of Error and Limitations . . . . .	38
7.1.2	Experimental Improvements . . . . .	40
7.2	Success Aspects . . . . .	41
7.3	Future Opportunities . . . . .	41
<b>8</b>	<b>Conclusion</b>	<b>42</b>
<b>References</b>		<b>46</b>
<b>A</b>	<b>Project Plan</b>	<b>47</b>
<b>B</b>	<b>Risk Register</b>	<b>49</b>
<b>C</b>	<b>Motors</b>	<b>51</b>
C.1	Brushed versus Brushless Motor Choice . . . . .	51
C.2	Aquatic Motor Choice . . . . .	51
C.3	Aerial Motor Datasheet . . . . .	54
<b>D</b>	<b>Unfolding Mechanism</b>	<b>55</b>
<b>E</b>	<b>Solenoid</b>	<b>57</b>
<b>F</b>	<b>Nose Cone</b>	<b>58</b>
<b>G</b>	<b>Waterproofing</b>	<b>60</b>
<b>H</b>	<b>Stabilization and Tail Fins</b>	<b>61</b>
<b>I</b>	<b>Battery and ESCs</b>	<b>62</b>
I.1	Battery . . . . .	62
I.2	Power Distribution . . . . .	63
<b>J</b>	<b>Wiring</b>	<b>65</b>

<b>K Radio and GPS</b>	<b>67</b>
<b>L Additional Electronic Material</b>	<b>69</b>
L.1 Aquatic Motor Running (link to video) . . . . .	69
L.2 Aerial Motors Running (link to video) . . . . .	69
L.3 Unfolding Mechanism Opening (link to video) . . . . .	69
L.4 Slow Motion Experiment (link to video) . . . . .	69
L.5 Associated CAD Files (link to drive) . . . . .	69
L.6 Raw Experiment Tracking Data (link to drive) . . . . .	69

# Notation

## Acronyms and Abbreviations

ABS	– Acrylonitrile Butadiene Styrene
AUV	– Autonomous Underwater Vehicle
BEC	– Battery Elimination Circuit
CAD	– Computer-Aided Design
ELF	– Extremely Low Frequency
ESC	– Electronic Speed Controller
FC	– Flight Computer
FDM	– Fused Deposition Modeling
FPS	– Frames Per Second
FPV	– First-Person View
GPS	– Global Positioning System
HF	– High Frequency
IMU	– Inertial Measurement Unit
LiPo	– Lithium-Ion Polymer
PETG	– Polyethylene Terephthalate Glycol
PID	– Proportional-Integral-Derivative
PLA	– Polylactic Acid
ROUV	– Remotely Operated Underwater Vehicle
ROV	– Remotely Operated Vehicle
RPM	– Revolutions Per Minute
SLAM	– Simultaneous Localization And Mapping
SPURV	– Special Purpose Underwater Research Vehicle
SRDRS	– Submarine Rescue Diving Recompression System
TRL	– Technology Readiness Level
UAAV	– Unmanned Aerial-Aquatic Vehicle
UAV	– Unmanned Aerial Vehicle
UHF	– Ultra High Frequency
UVU	– Unmanned Underwater Vehicle

# List of Figures

2.1	Quadcopter propeller spin directions and torques . . . . .	2
2.2	Special Purpose Underwater Research Vehicle (SPURV) . . . . .	3
2.3	Submarine Rescue Diving Recompression System (SRDRS) . . . . .	3
2.4	Folding (left) and unfolding (right) multi-modal propeller blades . . . . .	4
2.5	Microrobot aerial-aquatic transition. Left: water-entry; right: water-exit . . . . .	5
2.6	The Naviator UAAV pictured underwater . . . . .	5
2.7	The EagleRay UAAV pictured underwater . . . . .	6
2.8	The AquaMAV UAAV folding wing concept . . . . .	6
3.1	Three stages of motion: 1) aquatic; 2) transition; 3) aerial . . . . .	8
4.1	Side view of the final folded vehicle with three sections separated: a) aquatic section; b) electronics; c) aerial section . . . . .	10
4.2	Overview of the aerial section . . . . .	11
4.3	Chosen motor and propeller combination . . . . .	12
4.4	Labeled components of the unfolding mechanism . . . . .	12
4.5	Unfolding mechanism stages: a) fully folded; b) partially unfolded; c) fully unfolded . . . . .	13
4.6	Explored options to move the bottom runner upward: left: compression spring; right: tension rubber bands . . . . .	13
4.7	Hooks on top and bottom runners to hold the rubber bands in place . . . . .	14
4.8	Fracture point correctly predicted by simulation software . . . . .	14
4.9	Simulation of stress in frame arm before (left) and after increasing thickness (right) . . . . .	15
4.10	Initial concept design of the servo release mechanism . . . . .	15
4.11	Backlash in the mechanism causes the frame arms to protrude away from the central shaft. Red lines highlight the difference in angle between the locking pin and the central shaft . . . . .	16
4.12	Runner offset height . . . . .	16
4.13	Final form of the unfolding and servo release mechanisms with no frame arm protrusion	17
4.14	Overview of the aquatic section . . . . .	18
4.15	Generic aquatic propeller geometry . . . . .	18
4.16	Overview of the nose cone highlighting the locking fins . . . . .	19
4.17	Nose cone profile construction parameters . . . . .	20
4.18	Explored nose cone shapes . . . . .	20
4.19	Waterproof compartment consisting of seals on both sides of a hollow tube . . . . .	21
4.20	Design features of the waterproof seal . . . . .	21
4.21	Stabilizing tail fins surrounding the aquatic motor housing . . . . .	22
4.22	Diagram showcasing the primary vehicle electronics . . . . .	23
4.23	Overview of the electronics section . . . . .	24
4.24	Chosen power source: GNB 2600mAh 4S 110C LiPo Battery . . . . .	24

4.25	XT60W waterproof connectors outside the waterproof compartment to charge and disconnect the battery externally . . . . .	25
4.26	SpeedyBee F7 V3 BL32 50A 30x30 flight computer connected to a 4-in-1 ESC . . . . .	26
4.27	PID controller model used in this project . . . . .	26
4.28	Hole in aquatic motor housing allows for receiver wire to run out of the vehicle to the floating buoy . . . . .	27
5.1	Acrylic tubing roughness after cutting . . . . .	28
5.2	Waterproofing test of 3D printed seals, left: seam; right: wire entry hole . . . . .	29
5.3	Final assembly of the aerial-aquatic vehicle with nose cone removed (open state) . . . . .	30
5.4	Final assembly of the aerial-aquatic vehicle with nose cone (closed state) . . . . .	31
6.1	Consecutive snapshots showing Kinovea tracking the vertical position/velocity/acceleration of the aerial motor . . . . .	33
6.2	Relationship between the vertical position of the aerial motor and the time after the release of the unfolding mechanism . . . . .	33
6.3	Relationship between the elastic force on the unfolding mechanism and its opening time . . . . .	34
6.4	Relationship between the vertical velocity of the aerial motor and the time after the release of the unfolding mechanism . . . . .	35
6.5	Relationship between the vertical acceleration of the aerial motor and the time after the release of the unfolding mechanism . . . . .	36
7.1	The influence of high rubber band count on the vertical starting position. Left: 4 RB; Right: 14 RB . . . . .	37
7.2	A significant vertical offset 58 ms after releasing the servo during the 14 RB trial . . . . .	39
7.3	A frame-by-frame magnification (milliseconds since release indicated on top) showing the servo locking pin hugging the bottom runner during the 40-60 ms times (4 RB trial) . . . . .	40
A.1	Complete Gantt chart plan for the thesis project . . . . .	48
C.1	Comparison of brushless and brushed motor configurations . . . . .	51
C.2	Hybrid motor approach would increase drag on the vehicle due to protrusion of frame arms in order to produce vertical thrust . . . . .	52
C.3	Chosen motor and propeller combination . . . . .	52
C.4	Different parts of the aquatic propulsion system . . . . .	53
C.5	Aerial motor datasheet . . . . .	54
D.1	Improved unfolding mechanism geometry without bistability . . . . .	55
D.2	The force of the two runners colliding is transferred into the central shaft via the mounting bolt . . . . .	56
E.1	Inner workings of a simple solenoid pin locking device . . . . .	57
F.1	Separated nose cone pieces and labeled design intricacies . . . . .	58
F.2	Proof of being able to lower the vehicle by a wire through the top cutout in the nose cone . . . . .	59
G.1	Waterproofing on final vehicle . . . . .	60

I.1	Initial battery and electronic speed controller housing design . . . . .	63
I.2	ESCs, left: SpeedyBee BL32 50A 4-in-1 ESC; right: Hobbywing Skywalker 80A UBEC ESC . . . . .	63
I.3	Power distribution from battery to flight computer and motors . . . . .	64
J.1	Wiring from the aerial motors running along the frame arms into the hollow shaft . . . . .	65
J.2	Hollow shaft allows for motor wires with bullet connector ends to run down to the flight computer . . . . .	66
J.3	Wiring running from the bottom hole of carbon fiber rod into the waterproof compartment . . . . .	66
K.1	Jumper T Lite V2 Transmitter (ELRS) . . . . .	67
K.2	GPS module . . . . .	68

# List of Tables

B.1 Risk Register . . . . .	50
-----------------------------	----

# Word Count

<b>Chapter</b>	<b>Word Count</b>
Introduction	312
Literature Review	1204
Design Philosophy	649
Design	3881
Manufacturing and Assembly	711
Experiments and Results	1102
Discussion	1856
Conclusion	257
<b>Total</b>	<b>9972</b>

# Chapter 1

## Introduction

In recent decades, the usage of unmanned aerial vehicles (UAVs) has skyrocketed due to the ability they grant for human operators to access a medium that has traditionally required large and expensive equipment [1]. The elimination of onboard human presence is a key strength of UAVs which allows them to fly through tight spaces and perform agile and rapid maneuvers in the air. Operations such as search and rescue have begun taking advantage of the cost and time benefits of deploying UAVs to aid in locating individuals in distress or danger. UAVs are also being used in dangerous and remote environments such as on Mars, where NASA's Ingenuity UAV helicopter conducted an aerial observation of the Martian surface. The fields of rescue and exploration have seen revolutionary changes in their practices thanks to the high maneuverability and remote operability of UAVs. An extension to multi-modal operation, which would enable access to the underwater domain, could improve these vehicles further but would bring about new challenges. Existing research has focused on vehicles that transition slowly from the water surface into the air, which restricts the maneuverability of the UAV, losing a key reason for their adoption in many fields.

### 1.1 Aims

1. Design and manufacture a hybrid aerial-aquatic vehicle that is capable of maneuvering in both mediums.
2. Check the feasibility of the aggressive water surface-exit maneuver by measuring the opening times of the unfolding mechanism to characterize the relationship for other similar mechanisms.

### 1.2 Objectives

The objectives of the thesis are to:

1. Produce a working prototype design of the unmanned aerial-aquatic vehicle using computer-aided design (CAD) tools.
2. Manufacture the prototype and characterize it with additive manufacturing (3D printing).
3. Assemble a waterproof electrical system capable of powering the vehicle both underwater and in the air.
4. Establish radio communication with the vehicle in both mediums.
5. Tune a PID controller to enable the vehicle to hover steadily in the air.

# Chapter 2

## Literature Review

### 2.1 Unmanned Aerial Vehicles

UAVs, more commonly known as drones, originated from the military pursuit of "force multiplication", which is the use of technology to enhance the capabilities of its personnel [2]. By the end of the 20th century, UAVs became an essential part of military operations, and, as a result, research and development of drones progressed to a point where their adoption in the commercial market became viable [3]. The earliest UAVs were balloons that carried incendiary devices to target locations. These evolved through the 1900s to unmanned fixed-wing aircraft controlled by computers [4]. In modern times, the rapid improvement of small-scale electrical and power storage systems has led to quadcopter and helicopter UAVs' rise in prominence [5].

The control system of quadcopters is relatively simple to implement due to the motor configuration (see **Figure 2.1**). The simpler control system of quadcopters also allows for easier passive stabilization, which aids human operators during flight, making quadcopters the most common type of remotely controlled UAV in the world [6] and the choice of UAV for this thesis project.



Figure 2.1: Quadcopter propeller spin directions and torques [7]

Most quadcopters communicate with the operator using ultra-high frequency (UHF) radio communication protocols such as Bluetooth or WiFi [8, 9].

### 2.1.1 Quadcopter Applications

The lack of need for a runway, as well as other benefits such as autonomy and maneuverability, have enabled quadcopters to be used in wildlife monitoring [10], search and rescue [11], as well as for cartography to improve the resolution of maps [12]. Peristiowati et al. [13] have suggested the deployment of quadcopters in natural disaster areas to aid in monitoring the status of victims while rescue crews arrive. Unfortunately, quadcopters are highly limited when it comes to operation in or near the aquatic domain and hence their multi-modal development could strongly benefit many of their current application fields.

## 2.2 Unmanned Underwater Vehicles

There are two primary classes of Unmanned Underwater Vehicles (UUVs):

1. Remotely Operated Underwater Vehicle (ROUV)
2. Autonomous Underwater Vehicle (AUV)

These categories distinguish whether or not the vehicle is operated by a human or a computer algorithm. The first AUVs were classified in the 1950s when the U.S. created the Special Purpose Underwater Research Vehicle (SPURV) (see **Figure 2.2**), an aluminum hull, torpedo-shaped AUV, which communicated using acoustic waves and collected oceanographic data for over 20 years [14]. ROUVs such as the Submarine Rescue Diving Recompression System (SRDRS) (see **Figure 2.3**) have been used in underwater rescue efforts to save people from disabled submarines on the seafloor without risking large crews required to operate traditional rescue vehicles [15].



Figure 2.2: Special Purpose Underwater Research Vehicle (SPURV) [16]



Figure 2.3: Submarine Rescue Diving Recompression System (SRDRS) [17]

### 2.2.1 Autonomous Underwater Vehicle Operating Principles

Most AUVs opt to use a single motor with an underwater propeller to control the thrust of the vehicle and change the trim of control surfaces (fins) to adjust the direction of forward motion. A core part of achieving vehicle stability underwater is having a large distance between the center of gravity and the center of buoyancy, which is often achieved by positioning heavy components at the bottom of the vehicle and light components at the top [18]. Some UAVs, such as the Slocum Glider, have adapted highly efficient variable buoyancy propulsion, where a heavy battery is moved

to alter the center of gravity, traveling in a sawtooth trajectory and studying coastal waters for months at a time [19]. Due to the poor propagation of radio waves in water, AUVs communicate with remote control posts via acoustic signals. Additionally, the lack of Global Positioning System (GPS) availability underwater results in many AUVs having to deploy advanced self-localization algorithms such as "Simultaneous Localization And Mapping" (SLAM) to navigate and track their own location [20].

## 2.3 Unmanned Aerial-Aquatic Vehicles

One of the primary difficulties in developing successful Unmanned Aerial-Aquatic Vehicles (UAAVs) is the requirement to account for operation under both aerodynamic and hydrodynamic conditions when designing the vehicle [21]. The propulsion system of UAAVs is limited by the efficiency of propellers in a given medium [22]. Aerial propellers tend to rotate at much higher speeds compared to underwater ones and thus have very different shapes (pitch and diameter) [23]. This requires most UAAV vehicles to either sacrifice performance significantly in one of the mediums or to incorporate two separate propulsion systems, each of which becomes obsolete when switching to the other medium, effectively adding dead weight to both vehicle modes. Li et al. [24] have suggested a solution to the blade shape problem using passively morphing propellers that fold underwater and unfold in the air (see **Figure 2.4**).

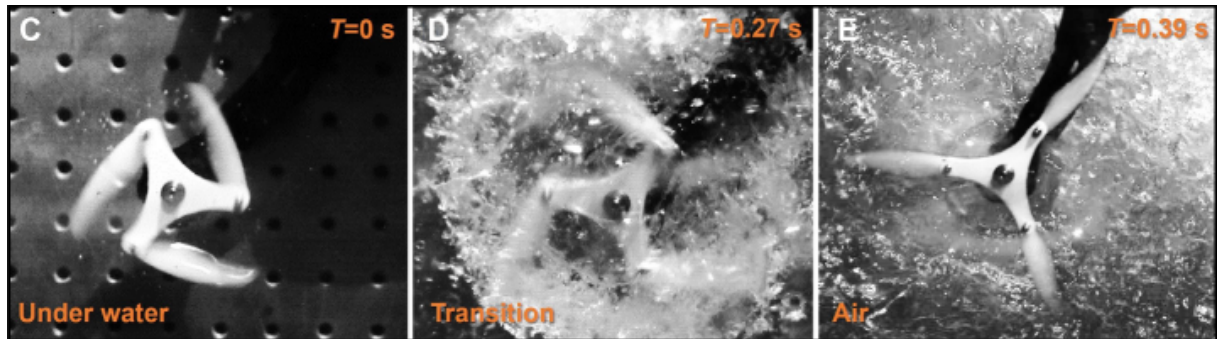


Figure 2.4: Folding (left) and unfolding (right) multi-modal propeller blades [24]

While these propellers have a fast deployment time (0.35s) and excellent stability, a significant limitation is the inability of the design to detect the state of adhesion of the blades, which means it can not ensure that the propellers remain folded while operating underwater.

### 2.3.1 Current Challenges in Medium Transition

As it stands today, the majority of vehicles that achieve multi-domain operation do so by executing a modal transition maneuver from the surface of the water into the air [21]. This sacrifices the maneuverability of the UAAV as it must first float to the water surface to break the surface tension and only then perform the transition maneuver.

Many UAAV medium transition mechanisms take inspiration from nature due to the ability of animals, such as cormorants and flying fish, to seamlessly transition between the aerial and aquatic mediums when diving for food or avoiding aquatic predators [21, 25]. While breaking the surface tension of water can be difficult, especially for small-scale vehicles, Chen et al. [26] demonstrated that this could be done using a UAAV microrobot which is inspired by the whirligig beetle (see **Figure 2.5**).

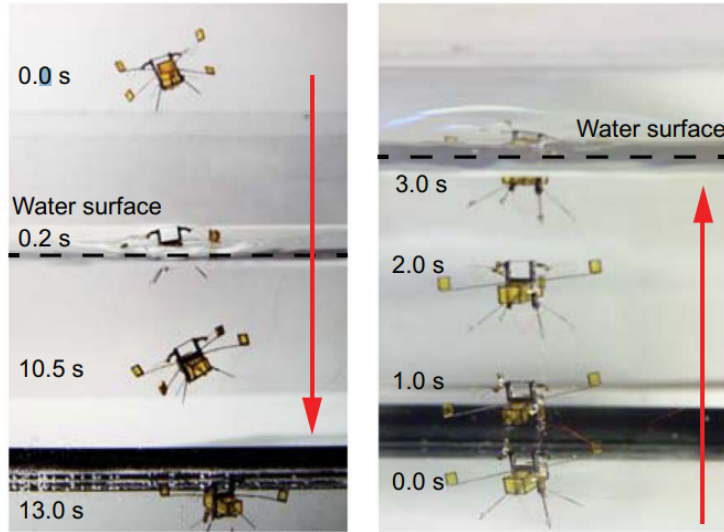


Figure 2.5: Microrobot aerial-aquatic transition. Left: water-entry; right: water-exit [26]

Mintchev and Floreano [27] explore how birds change the shape and orientation of their wings (via retraction) to adapt to higher density and viscosity when diving into the water for food.

Since the non-waterproof cavities of the UAAV are filled with water during the underwater phase of operation, the medium transition maneuver must also consider the passive or active egress of any carried water when entering the air. This is because underwater motors require less thrust compared to aerial motors (as a result of buoyancy reducing the effective weight of the vehicle when underwater). The aerial mode of the UAAV must therefore be as light as possible [28].

### 2.3.2 Current UAAV Prototypes

While most of the research surrounding UAAVs focuses on dynamics modeling, there have been some manufactured prototypes such as the Navigator, a hybrid quadcopter designed by Maia et al. [29] (see **Figure 2.6**). This UAAV utilizes an octo-quadcopter configuration where each set of four propellers is optimized for each domain and remains in fixed positions above and below the drone. The drawback of this UAAV is that it does not benefit from having a slender shape underwater, which would aid in high-speed maneuvering, and instead has a fixed drone body which is designed for aerial stability.

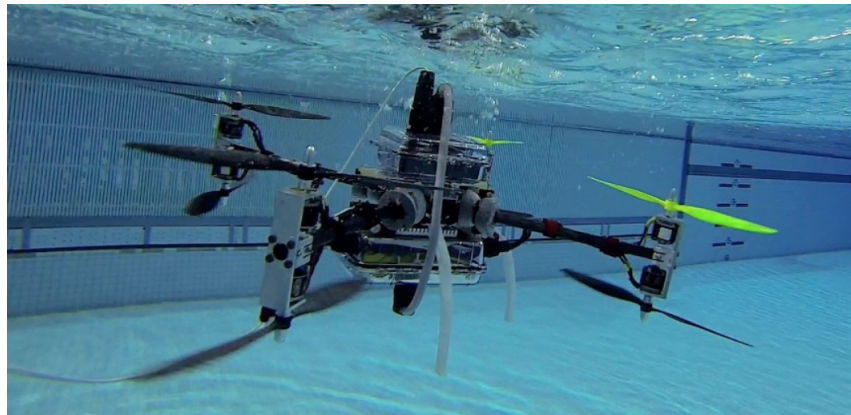


Figure 2.6: The Navigator UAAV pictured underwater [29]

The EagleRay UAAV prototype by Weisler et al. [30] encountered similar underwater movement limitations due to its fixed-wing aircraft-like design (see **Figure 2.7**). The EagleRay was measured to have a velocity drop of over 90% when transitioning into the water.

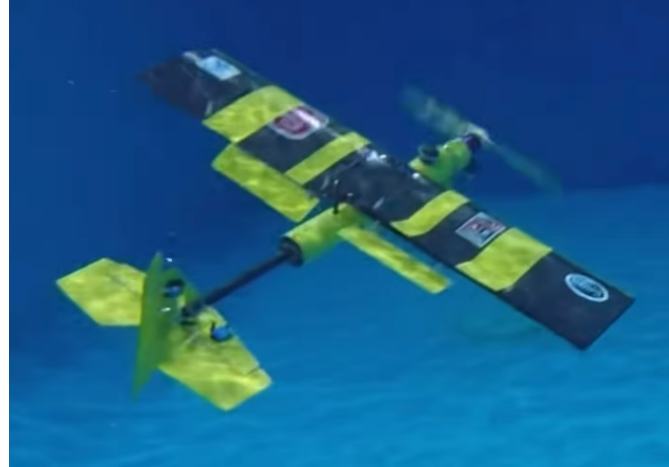


Figure 2.7: The EagleRay UAAV pictured underwater [30]

Another example of a manufactured UAAV prototype is the AquaMAV, a gannet (seabird) inspired folding wing vehicle built by Siddall and Kovač [28] (see **Figure 2.8**). The AquaMAV prototype was able to propel itself 4.8 m into the air (about 72 times its size) piercing the surface of the water, using a jet propulsion system.

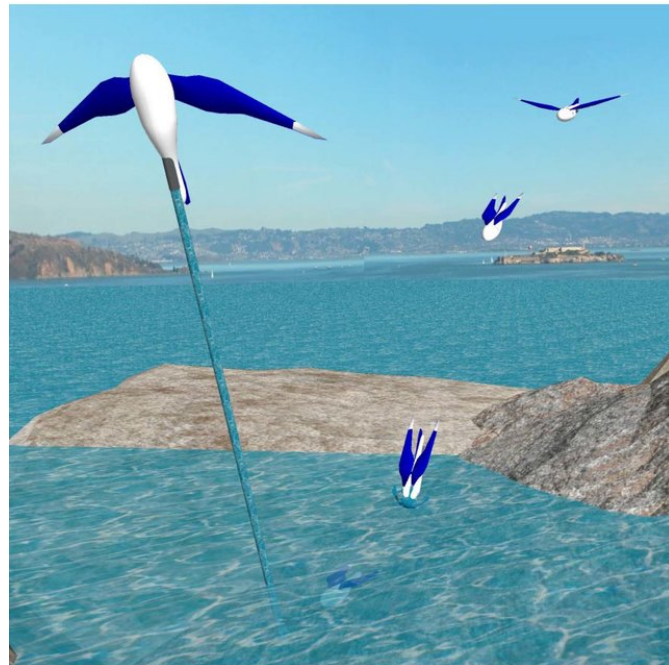


Figure 2.8: The AquaMAV UAAV folding wing concept [28]

# Chapter 3

## Design Philosophy

This chapter covers the approaches, constraints, resource limitations, and design priorities used to guide the decision-making when executing the project and producing the prototype vehicle. Below is a brief summary of the key considerations used to ensure that the vehicle could be finished within the 3-month long project timeline:

1. Demonstrating the functionality of the vehicle is critical and its form factor or aesthetics should not be prioritized.
2. Simplicity and straightforward design are crucial for the successful completion and documentation of all parts of the vehicle.
3. Modular design ensures that anyone seeking to extend this project in the future can choose to modify individual vehicle components without drastically changing the overall conceptual design.
4. Rapid prototyping and iteration should be prioritized over efficiency and optimized performance.

### 3.1 Evaluation Methods

Since the primary goal of this thesis is to demonstrate the viability of a rapid water-to-air transition maneuver, it is critical to consider what constitutes a viable maneuver and how it can be evaluated quantitatively and qualitatively upon completing the prototype build. A bottom-up engineering approach was taken, whereby the viability of each subsection of the maneuver would be evaluated separately. With this approach, a malfunction in the final test could be isolated to be a fault or failure in a specific section of the maneuver or vehicle, which would simplify the troubleshooting process. On the highest level, the maneuver was broken down into the following three stages of motion (see **Figure 3.1**):

1. Maneuvering in the water and up to the surface.
2. Completing a water-to-air transition and rapidly deploying aerial propellers to produce lift for the vehicle to maintain its altitude.
3. Demonstration of the vehicle's ability to maintain stable flight after completing the transition maneuver.

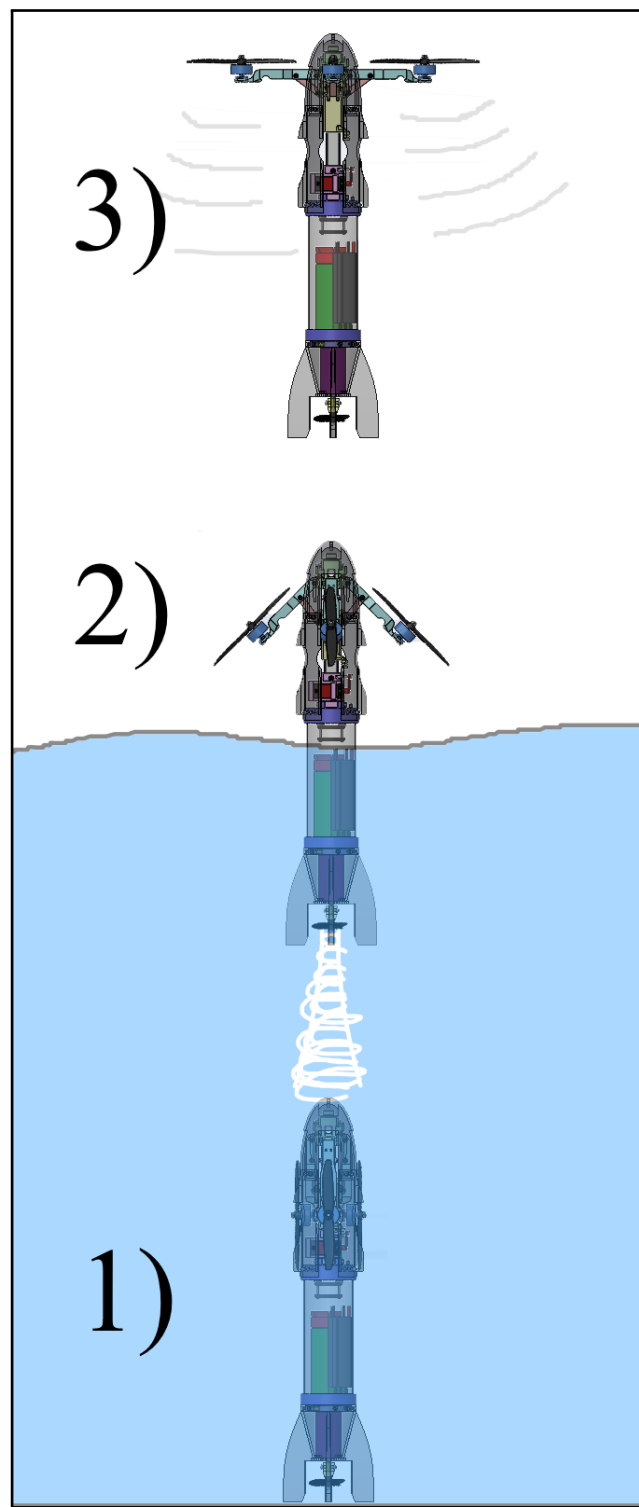


Figure 3.1: Three stages of motion: 1) aquatic; 2) transition; 3) aerial

Furthermore, the scope of the project was limited by a number of factors such as available equipment, time, and facilities. These were evaluated before starting the conceptual design process in order to determine which parts of the vehicle's motion and capabilities required constraints. A detailed plan was put in place to achieve the stated goals of the project (see **Figure A.1**).

## 3.2 Testing Facility

The university's FloWave Ocean Energy Research Facility, which contains a 25m diameter and 2m deep circular basin of water surrounded by concrete, was chosen to be the eventual location for validating the complete rapid water-exit maneuver. In case the FloWave facility became unavailable or inaccessible, a contingency plan was made to conduct the full-scale test at an alternative facility, which was approximately the same depth (2-4 meters).

## 3.3 Motion Constraints

To simplify the stages of motion, it was determined that the vehicle would be designed to start in a vertical orientation at the bottom of the water pool (similar to a traditional rocket) and only accelerate vertically using a single underwater motor until it exits the water surface. Hence, the focus of the thesis could remain on manufacturing a viable testing prototype within the project timeline. There was, however, one major challenge with this simplification: maintaining a vertical attitude during the vehicle's ascent. This concern is addressed in **Section 4.2.4**.

Additionally, it was decided that after the vehicle completes the transition maneuver, its aerial motion should be simplified to a momentary hover at a constant position in the air, which would sufficiently demonstrate that it can achieve stable flight after the rapid transition. After the short hover, the vehicle would turn off and fall back into the water below it.

## 3.4 Risks and Mitigation

The risks which could lead to failure to complete the project within the allocated time frame were carefully assessed and discussed with the thesis supervisor before starting the project. A risk register (see **Table B.1**) was made to outline some of the key risks and their mitigation procedures so as to maintain the timely progress of the project.

# Chapter 4

## Design

The design of the prototype aerial-aquatic vehicle is the most important and extensive part of this project. In order to properly and completely understand the full design, it must be broken down into its constituent parts, the primary of which are: the aerial section, the aquatic section, and the electronics. Each of these three sections (see **Figure 4.1**) is responsible for performing a set of tasks to enable the full maneuver to be executed.

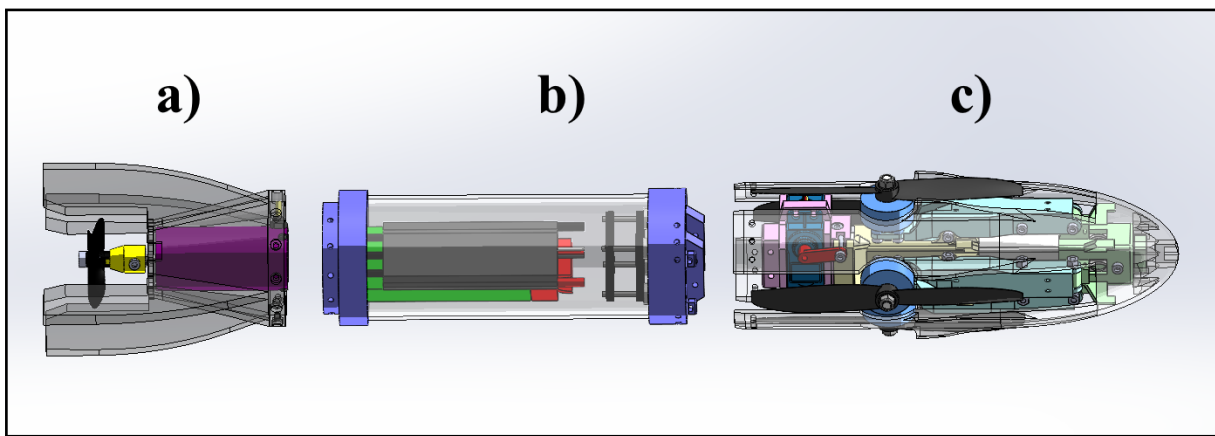


Figure 4.1: Side view of the final folded vehicle with three sections separated:  
a) aquatic section; b) electronics; c) aerial section

### 4.1 Aerial Section

The aerial section of the vehicle is responsible for the aerial transition and flight. It includes an unfolding mechanism, release mechanism, aerial motors, and aerial propellers. The release mechanism moves a bolt which allows the tension in the unfolding mechanism to pull the aerial motors and propellers out of an aquatic configuration into an X-frame (aerial configuration). Once opened, this configuration functions much like a traditional quadcopter.

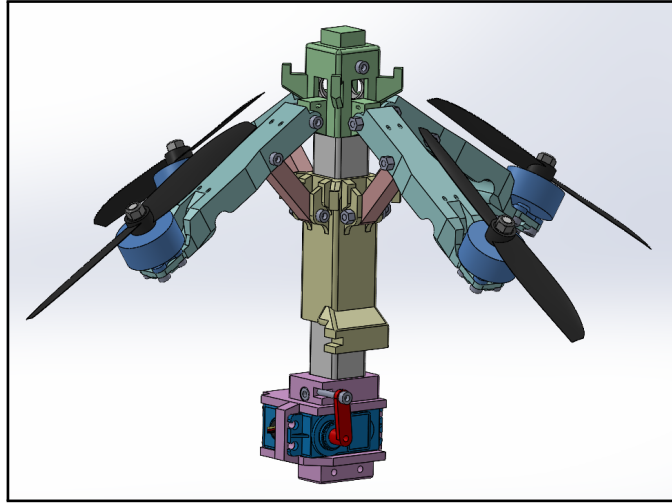


Figure 4.2: Overview of the aerial section

### 4.1.1 Aerial Motors and Propellers

The first decision when it came to designing the aerial section was the selection of appropriate motors and propellers. It was decided early on that the vehicle would consist of four separate aerial motors and a single aquatic motor (discussed in **Section 4.2.1**). Each of these motors would only propel the vehicle in their respective mediums. The reason for choosing four aerial motors was the simplicity of controlling and stabilizing such an aerial configuration. The downside of using separate motors for each medium was that the vehicle would have to carry the unused motor(s) as dead weight.

Before choosing electrical components it was important to acknowledge that the choice of exact motor type (see **Appendix C.1**) and model ultimately depended on local availability within a set of required specifications.

The first step was to estimate the total mass of the vehicle based on preliminary research into the various components which would contribute to the weight of the drone, namely the battery, electronic speed controllers (ESCs), and structure of the vehicle. Ultimately, it was determined the vehicle would weigh between 1.5 to 2 kg. The mass budget for the vehicle was therefore set at 2 kg. Even though the vehicle's flight profile was a basic hover, it would require more thrust than its weight due to utilizing the horizontal component of the thrust to stabilize the drone along its hover plane. Liang [31] mentions that generally, most drones aim to be able to produce about double the thrust compared to the weight of the vehicle to allow for sufficient maneuverability. A motor and propeller combination which would produce a peak thrust force of about 40 N was therefore chosen.

When it came to propeller choice, the diameter and number of blades were considered. The blades would have to sit seamlessly along the edges of the vehicle for it to stay slim and folded during its aquatic ascent. Propellers with three or more blades would be difficult to fold into the center of the vehicle as their swept areas may overlap. Thus, dual-blade propellers were chosen. Having two blades is also the most efficient number for an aerial propeller [32]. The longer the blades are, the more thrust the propeller produces. Despite this, longer propellers have the disadvantage of requiring a larger frame size, which in turn requires more torque to unfold. The propeller diameter was therefore chosen primarily based on what was recommended to go along with the chosen motor. Liang [33] compiled a table containing common motor and propeller combinations. This included columns to match the number of propeller blades, propeller size, and battery cell count to a desired

motor's revolutions per minute (RPM). Based on this information, the iFlight XING2 2306 2555 KV was found to be a suitable candidate for the project with 15 cm diameter and 10.7 cm pitch dual blade propellers (see **Figure 4.3**).

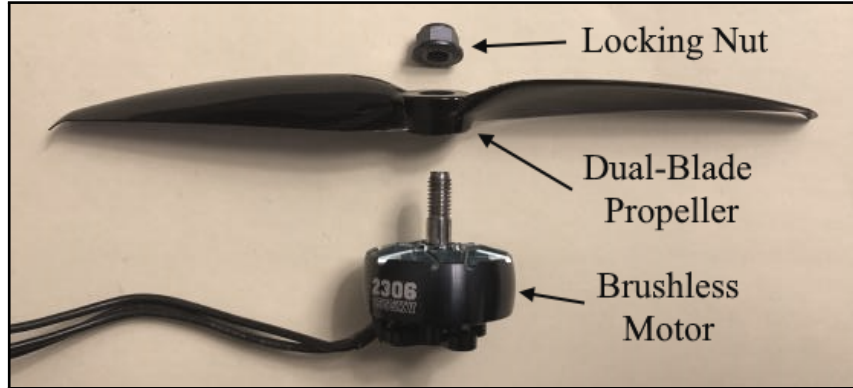


Figure 4.3: Chosen motor and propeller combination

According to the manufacturer (see **Figure C.5**), the chosen motor could achieve a peak thrust force of up to 12 N (totaling 48 N for all four motors) when set to max throttle with 50 A of current while using smaller 12.7 cm diameter dual-blade propellers, ensuring a safe margin of adequate thrust for hovering.

#### 4.1.2 Unfolding Mechanism

In order to shift the aerial propellers from an aquatic configuration to an aerial configuration, the vehicle uses a moving runner-based unfolding mechanism, much like common umbrellas. This consists of five parts: the top and bottom runners, the frame arm, the runner arm, and the central shaft (see **Figure 4.4**).

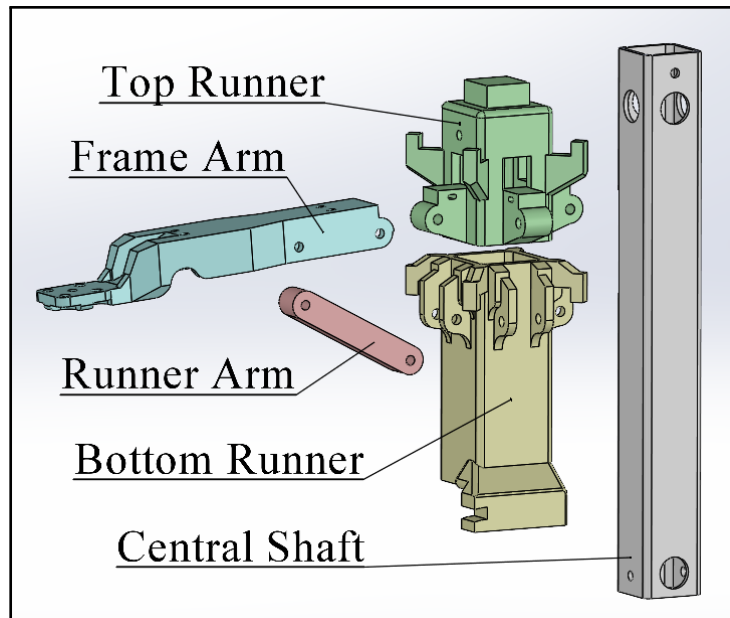


Figure 4.4: Labeled components of the unfolding mechanism

By fixing the top runner, and allowing the bottom runner to move up and down the central shaft, the frame arms pivot around their connection point to the bottom runner. This results in the frame arm being moved outward from its folded position effectively transforming the vehicle from a torpedo-like to quadcopter-like configuration. To find out more design considerations related to the unfolding mechanism, see **Appendix D**.

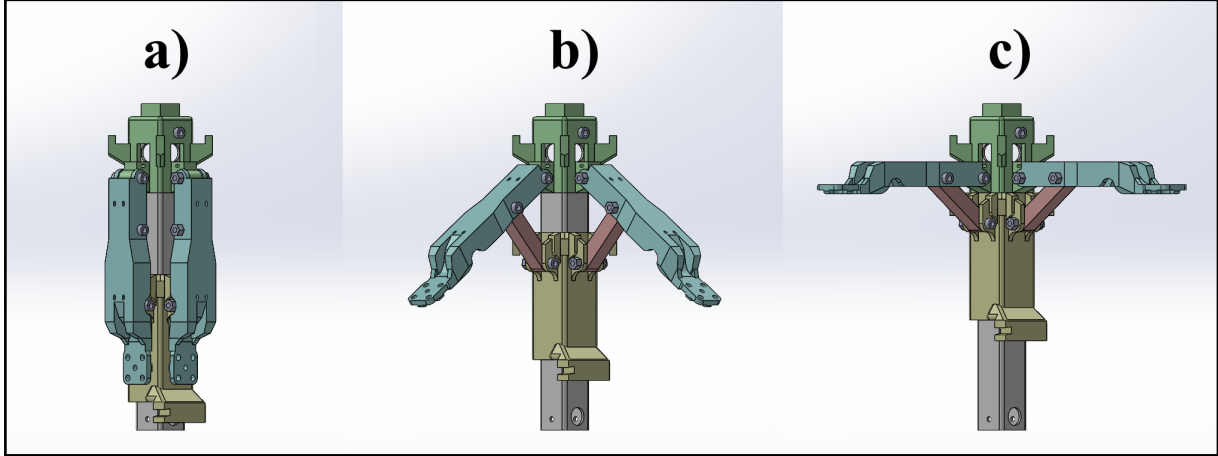


Figure 4.5: Unfolding mechanism stages: a) fully folded; b) partially unfolded; c) fully unfolded

In order to move the bottom runner toward the top runner two methods were explored. Since the unfolding mechanism was inspired by umbrella designs, the obvious first choice was to consider a spring. The spring would be compressed below the bottom runner and upon release would push it toward the top runner. The chosen alternative to springs was the use of rubber bands which are in tension to pull the runners toward each other (see **Figure 4.6**).

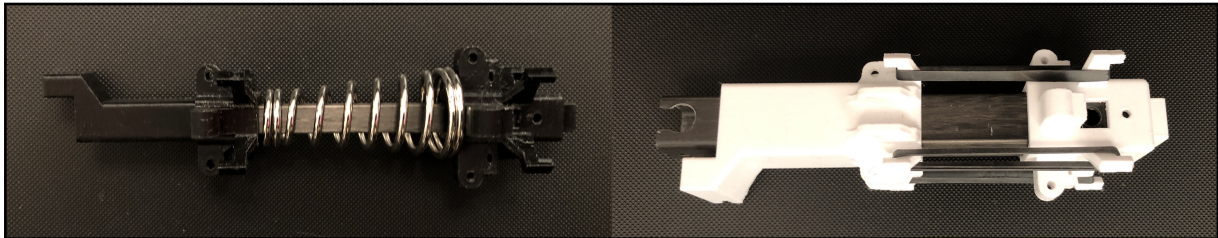


Figure 4.6: Explored options to move the bottom runner upward: left: compression spring; right: tension rubber bands

Rubber bands are usually avoided in industrial contexts due to their tendency to vulcanize over time, causing them to harden and lose their ability to stretch [34]. Despite this property, rubber bands proved to have a significant advantage compared to springs in that the stiffness of the system could be better tuned to match the design requirements by adding additional rubber bands. If a spring did not provide sufficient force to open the mechanism, it would likely have to be replaced, which may require redesigning the entire mechanism around a spring of different dimensions. The rubber bands were attached to the runner by adding vertically aligned hooks on each of the runners (see **Figure 4.7**).

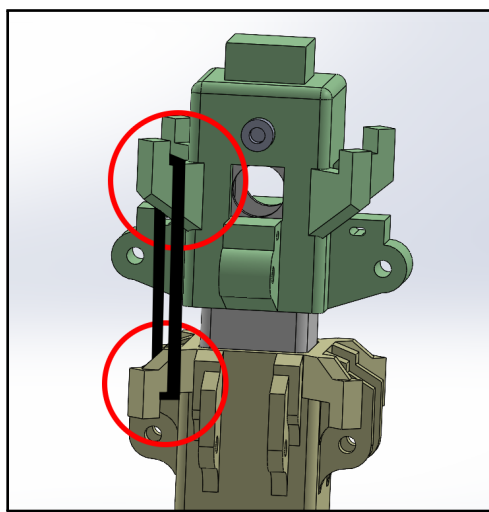


Figure 4.7: Hooks on top and bottom runners to hold the rubber bands in place

Upon testing the frame arms, it was found that they were too fragile to withstand the force of only four rubber bands (one on each hook) and fractured upon the collision of runners (see **Chapter 6** for the force of this collision). Conducting a SolidWorks stress study on the frame arms correctly found the fracture point to be on the underside of the arm, which matched the outcome of the tests (see **Figure 4.8**).

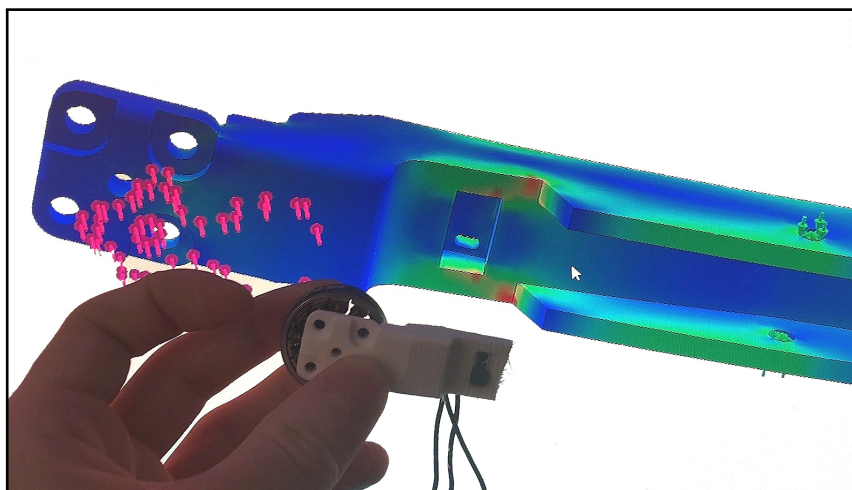


Figure 4.8: Fracture point correctly predicted by simulation software

The SolidWorks stress simulation was used to aid in redesigning the frame arms with increased thickness among other strengthening improvements. The new design (see **Figure 4.9**) was sufficiently strong to withstand up to 15 rubber bands, which would provide more than enough force for the mechanism to open impulsively (proven in **Section 6.1**).

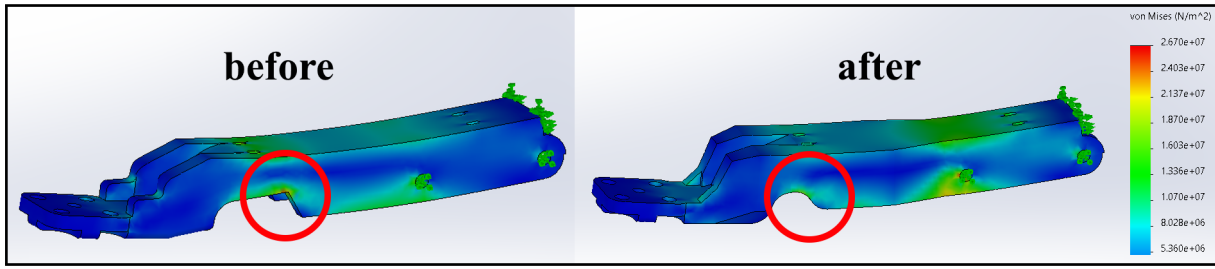


Figure 4.9: Simulation of stress in frame arm before (left) and after increasing thickness (right)

### 4.1.3 Release Mechanism

For the release mechanism, a servomechanism (henceforth shorted to servo) was used (see **Appendix E** for an alternative). Servos with high-output torques could overcome the normal force between the runner and a pin that would hold the runner in place. Their widespread use also made waterproofed servos readily available, which meant that the release mechanism would not have to be waterproofed manually later. The servo used in this vehicle is an FT5330M with a maximum torque of 35 kg·cm. When considering how to convert the rotational motion of the servo arm to a linear motion of a locking pin, a simple pivoting shaft was first considered (see **Figure 4.10**).

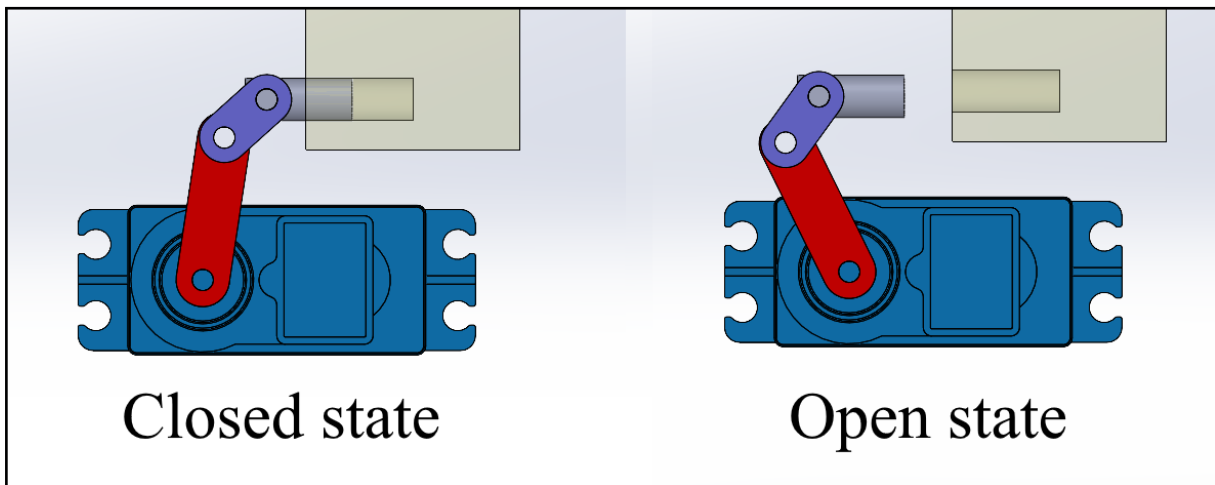


Figure 4.10: Initial concept design of the servo release mechanism

The issue with this mechanism became quickly apparent as the frame arms would stick out from the center of the vehicle in the aquatic configuration (see **Figure 4.11**). This was problematic as it would significantly increase the drag on the vehicle while moving through the water. The protrusion resulted from a combination of hidden problems. Firstly, the tolerance on the runner holes was too large which allowed the bolts connecting the runners and frame arm to move slightly, which created a backlash in the system. More importantly, however, the pin inside the bottom runner hole would get pulled up by the rubber bands, which allowed the bottom runner to move slightly, causing the frame arms to protrude outward.

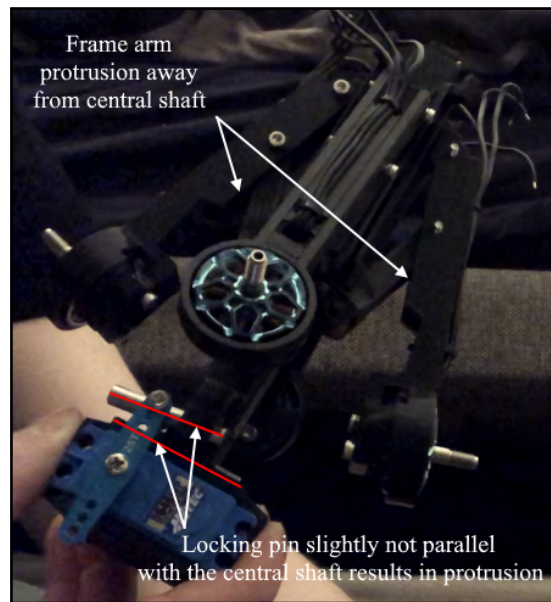


Figure 4.11: Backlash in the mechanism causes the frame arms to protrude away from the central shaft. Red lines highlight the difference in angle between the locking pin and the central shaft

In order to eliminate this backlash the design was altered in the following two ways:

1. The pin shaft shown in **Figure 4.10** was eliminated in favor of a locking bolt which would only move upward through bending instead of pivoting as was the case with the shaft.
2. The bottom runner height was adjusted such that the position of the locking bolt channel would be slightly higher than it should be (see **Figure 4.12**). This made it so that the bottom runner would have to be pulled down further, which would create increased tension in the mechanism.

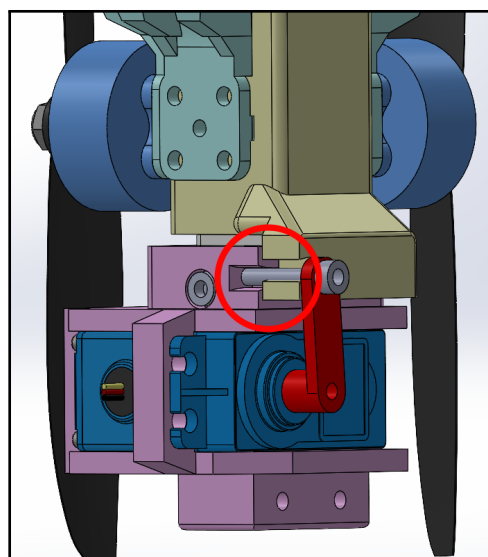


Figure 4.12: Red circle highlights the offset height of the bottom runner to add additional tension into the system and remove frame arm protrusion

As seen in **Figure 4.13**, these changes entirely removed the frame arm protrusion when testing with four to eight rubber bands.

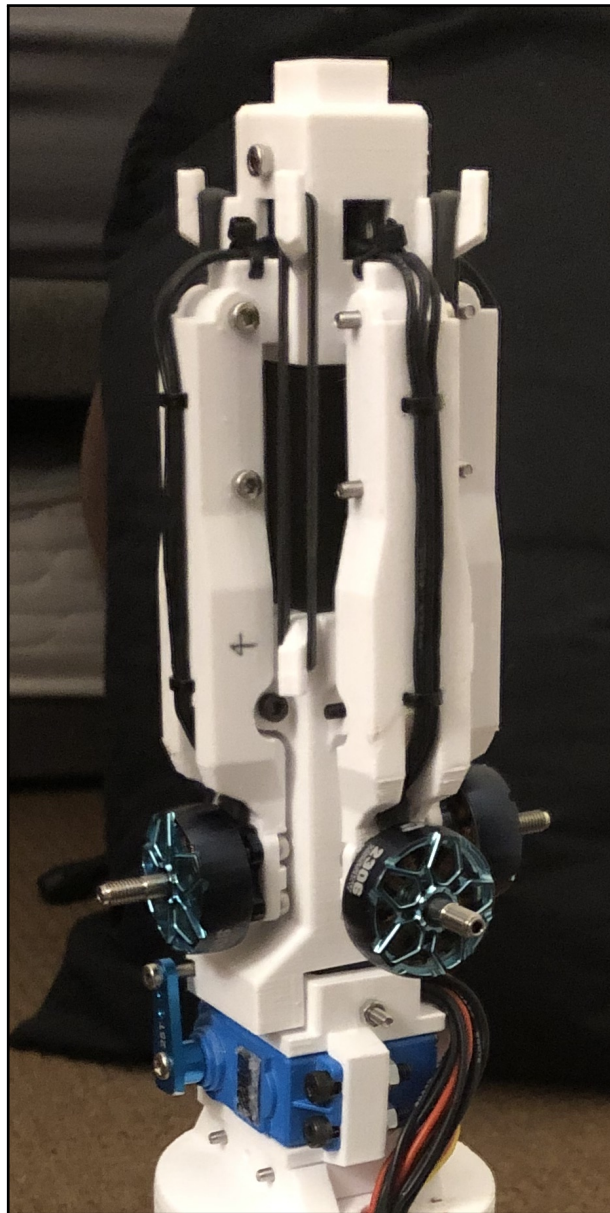


Figure 4.13: Final form of the unfolding and servo release mechanisms with no frame arm protrusion

## 4.2 Aquatic Section

The goal of the aquatic section is to propel the vehicle vertically upward through the water with enough acceleration to get it above the surface. This is then followed by the unfolding mechanism deploying and the vehicle transitioning to flight (see **Figure 3.1**). This section includes the nose cone, aquatic seals, tail fins, aquatic motor, and aquatic propeller.

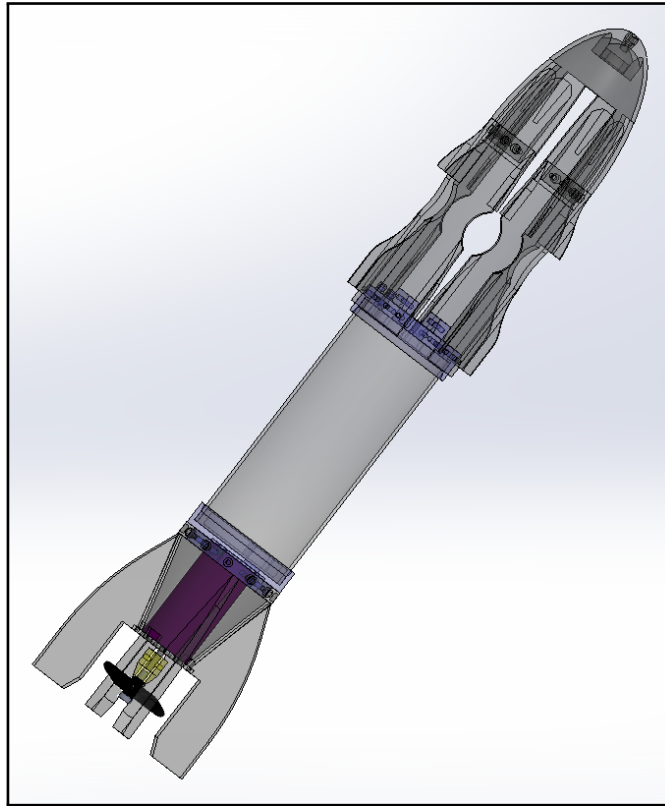


Figure 4.14: Overview of the aquatic section

### 4.2.1 Aquatic Motor and Propeller

The following considerations had to be made when choosing an aquatic motor and propeller. Aerial propellers are mounted perpendicular to the blade hub, whereas aquatic propellers are slanted by an amount referred to as the rake angle (see **Figure 4.15**). This is because most aquatic propellers of this scale are sold for hobby boats that lift the bow when maneuvering in the water. The rake angle on a propeller helps hold the water better as the boat is thrown up in the air. For this project, however, most of the aquatic ascent would occur under full submersion in water, which meant that a propeller with no rake would be optimal for better underwater stability [35].

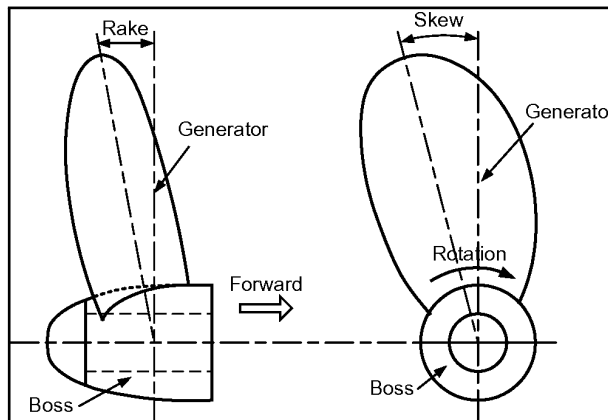


Figure 4.15: Generic aquatic propeller geometry [36]

The specifications of the chosen motor (Turnigy XK3674-2200KV 1750w Brushless Inrunner) were estimated to meet the thrust requirement based on its use in other similar applications [37]. For more information relating to the aquatic motor choice and its mounting, see **Appendix C.2**.

#### 4.2.2 Nose Cone

The nose cone fitted on top of the aerial section serves multiple purposes. The unfolding mechanism has many uneven surfaces which would disturb the flow of water during the aquatic ascent. To prevent this, the nose cone helps reduce drag on the vehicle by streamlining the flow of water across its surface. It also allows for protruding locking fins to be placed on the sides of the aerial propellers (see **Figure 4.16**), which act as barriers to prevent them from rotating freely before the aerial transition, further reducing drag. Additionally, the nose cone acts as added protection in case of a collision with any external surfaces during testing.

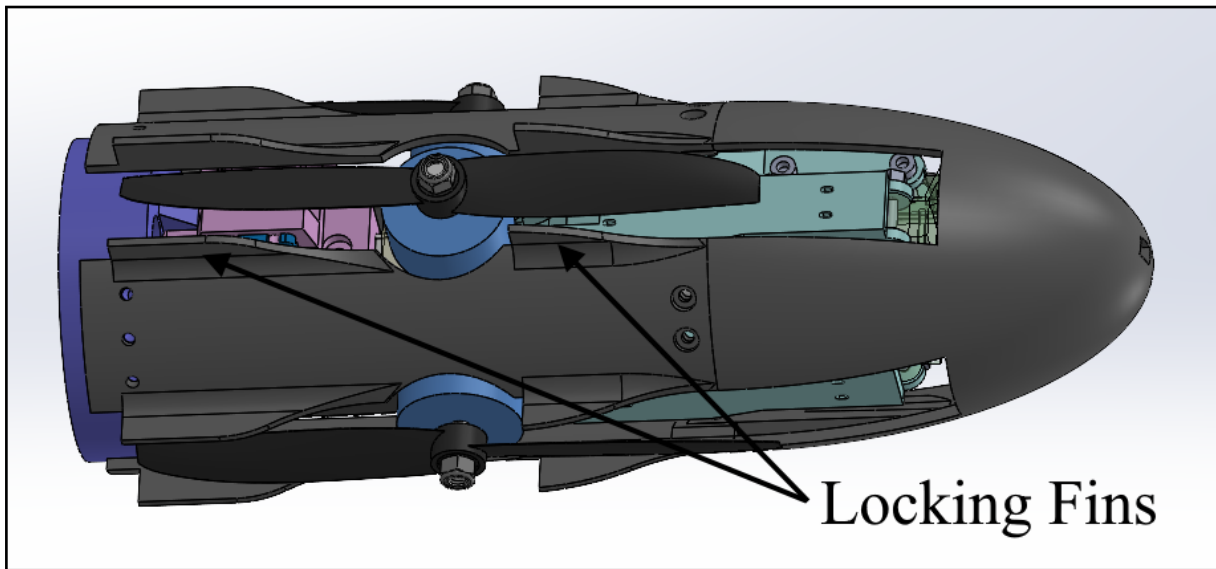


Figure 4.16: Overview of the nose cone highlighting the locking fins

When designing the nose cone, multiple different shapes were considered (see **Figure 4.18**). Vehicles that travel at speeds below Mach 0.8 (274.4 m/s) essentially do not experience pressure drag. This means that the primary contributor to drag on the vehicle is friction drag, which increases with the wetted area of the nose cone. Other factors which contribute to the magnitude of friction drag include shape discontinuities and the smoothness of the used material. According to Rajan [38], the best nose cone shape for subsonic vehicles is usually a smooth and short prolate hemispheroid (elliptical shape). This shape is governed by **Equation (4.1)**, where the parameters correspond to those shown in **Figure 4.17**.

$$y = R \sqrt{1 - \frac{x^2}{L^2}} \quad (4.1)$$

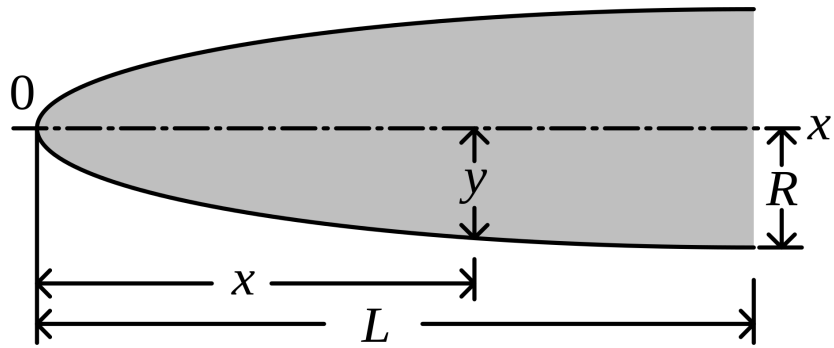


Figure 4.17: Nose cone profile construction parameters [39]

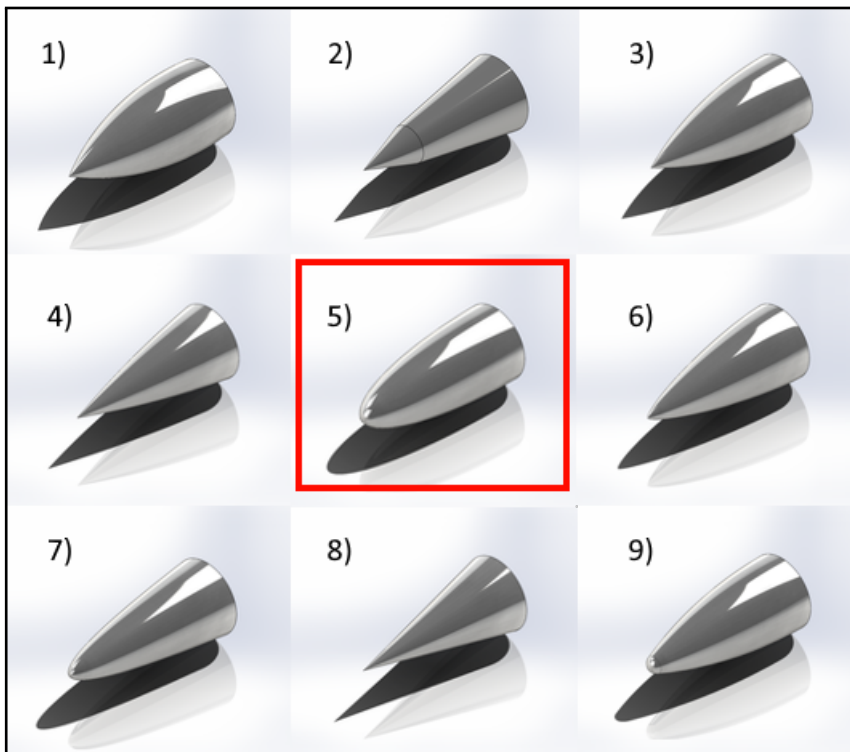


Figure 4.18: A selection of possible nose cone shapes: 1) Secant ogive; 2) Bi-conic; 3) Tangent ogive; 4) Parabolic; 5) Elliptical (chosen); 6) LD-Haack (Von Kármán); 7) Power series; 8) Conic; 9) Spherically blunted tangent ogive [40]

For more details about the nose cone design intricacies see [Appendix F](#).

### 4.2.3 Aquatic Seals and Waterproofing

For the vehicle to operate successfully underwater, design considerations had to be made in regard to waterproofing the electronics which would malfunction otherwise. Exceptions to this were the release servo, the aerial motors, and the aquatic motor, which was all chosen specifically to be waterproof without requiring any manual modifications. Seeing as the flight computer and inertial measurement unit (IMU) would have to be attached to the vehicle, there would still need to be a compartment that was waterproof. This compartment would also have to house the lithium polymer

battery which provided the vehicle with power. Since the battery was long (12 cm), the length of the vehicle was extended significantly as seen in the previous renders. To accommodate this length, an acrylic tube that fit all the wiring and electrical components was used. The choice of acrylic was due to its capability to resist water permeation, good impact strength, abundant availability, and ease of processing. The tubing was capped on both sides with 3D printed pieces to seal the compartment (see **Figure 4.19**).

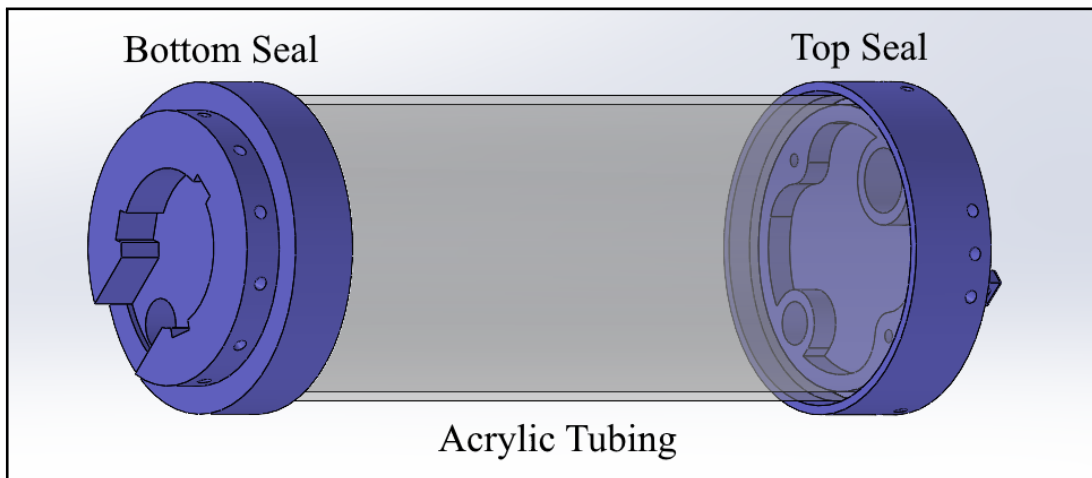


Figure 4.19: Waterproof compartment consisting of seals on both sides of a hollow tube

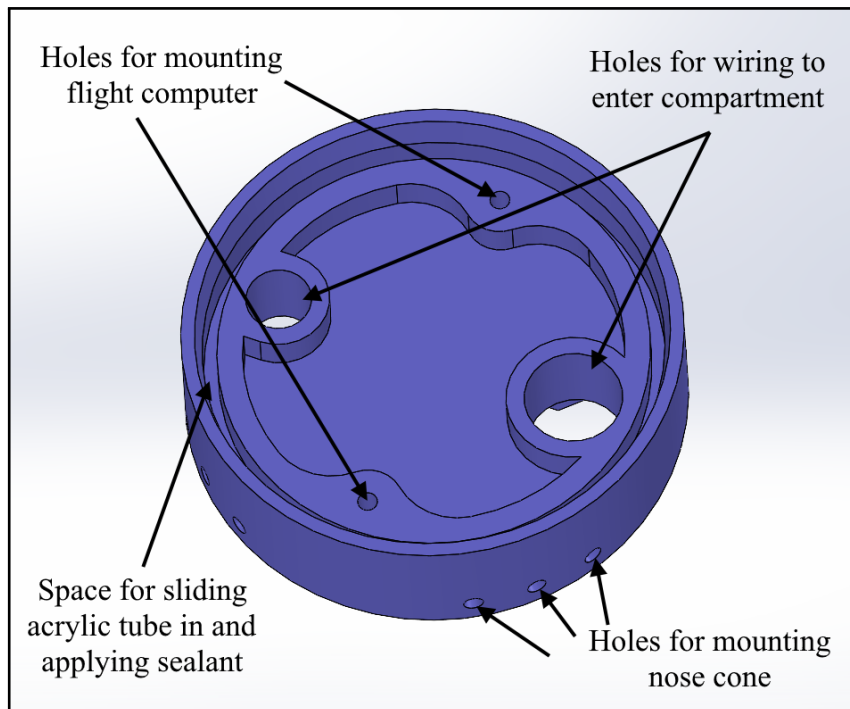


Figure 4.20: Design features of the waterproof seal

**Appendix G** describes the choice of waterproofing method and material in further detail.

#### 4.2.4 Stabilization and Tail Fins

Due to the lack of available time to implement an active stabilization system, this project opted for the use of large tail fins to passively stabilize the vehicle by lowering its center of pressure (see **Figure 4.21**).

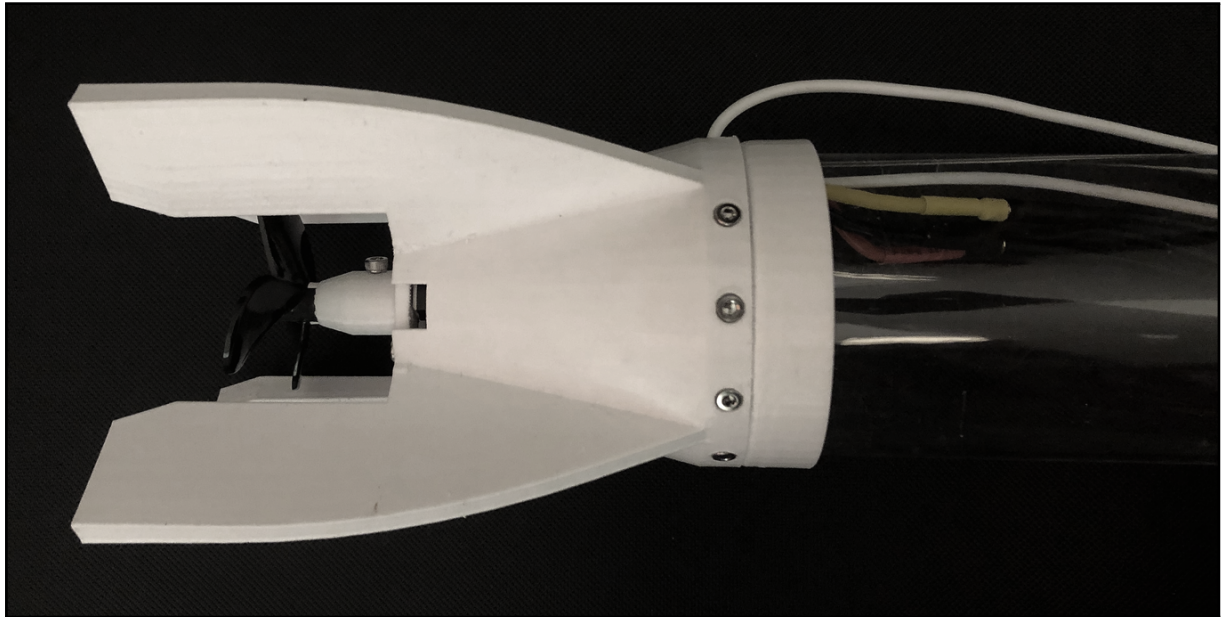


Figure 4.21: Stabilizing tail fins surrounding the aquatic motor housing

For further information on the passive stabilization fins, please see **Appendix H**.

Other than stabilization, the tail fins also serve two other purposes. Firstly, they act as legs for the vehicle to stand on. Seeing as the planned maneuver would only ascend vertically in the water, the vehicle would need to start pointing directly upward. Secondly, the tail fins protect the propeller and motor from breaking in case of an impact. The design was made in such a way that the propeller is unable to reach any external surfaces due to the "cage" formed around it by the tail fins (see **Figure 4.21**). Since the RPM of the motor is so high, even a simple fall without this protection would likely destroy the plastic propeller.

## 4.3 Electronics

The electronics section is responsible for listening to arming commands, powering the aerial and aquatic motors at the appropriate times, controlling the unfolding mechanism deployment, as well as stabilizing the vehicle during its aerial hover. It consists of a battery, flight computer, electronic speed controllers, radio transmitter/receiver, and GPS. Since the servo and all the motors were located outside of the waterproof compartment (due to already being waterproofed), they are omitted from this section and instead discussed in their respective chapters.

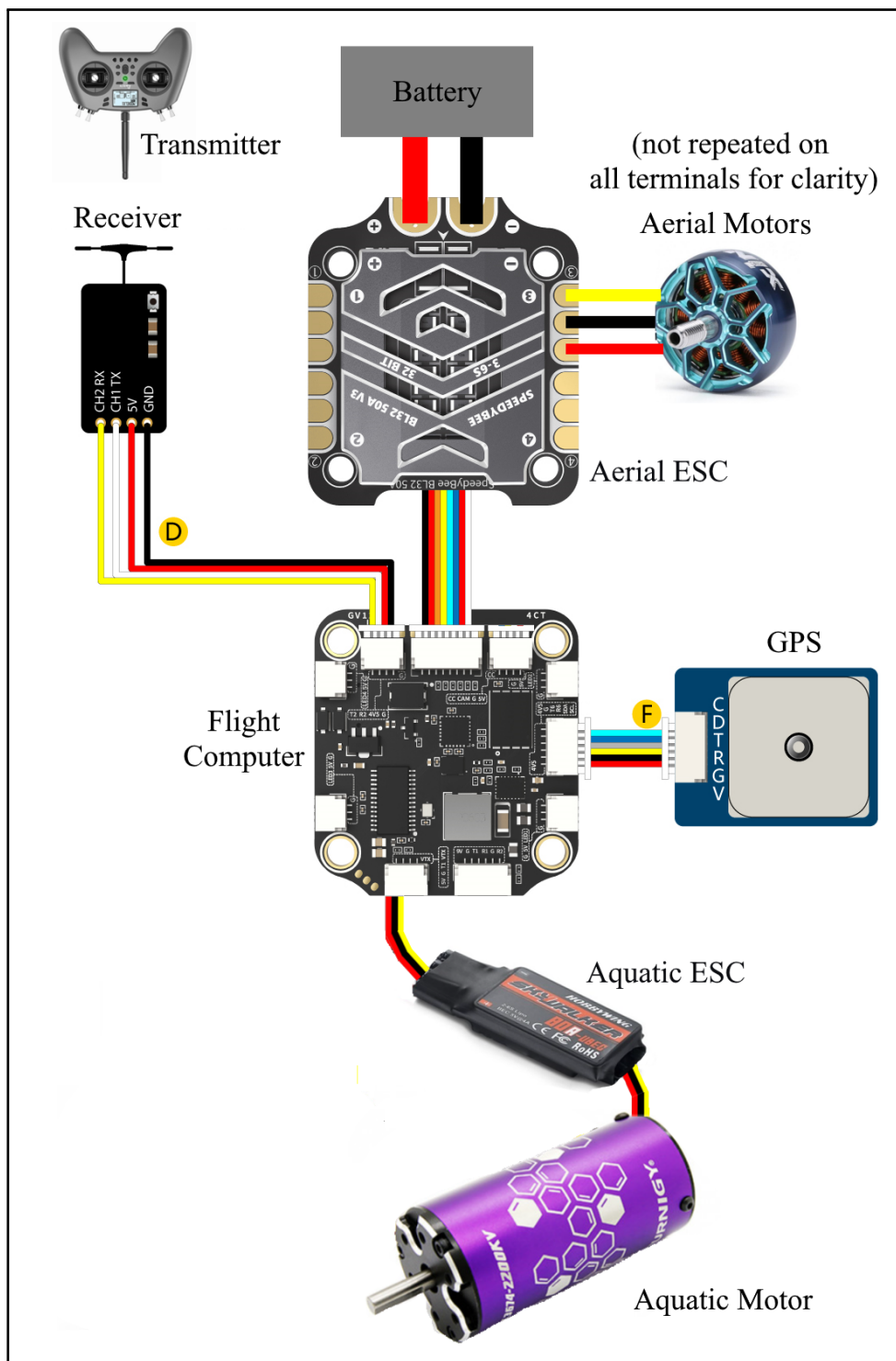


Figure 4.22: Diagram showcasing the primary vehicle electronics



Figure 4.23: Overview of the electronics section

### 4.3.1 Battery

Since the mass budget estimation accounted for the weight of a battery, it was decided that in order to keep the vehicle as autonomous and maneuverable as possible, a lithium polymer (LiPo) battery (see **Figure 4.24**) would be housed in the waterproof compartment.



Figure 4.24: Chosen power source: GNB 2600mAh 4S 110C LiPo Battery

According to the manufacturers, all the motors were ideally suited for operation with a 4S battery (14.8 V) [41, 42], which is the justification for the chosen cell count. Additionally, the aerial and aquatic motor(s) were capable of drawing a maximum current of 50A and 70A respectively. To see the considerations and calculations done prior to choosing the battery and power management devices (ESCs), see **Appendix I**.

## 4.4 Wiring

While it may seem trivial, routing the wiring from the aerial motors into the waterproof electronics compartment turned out to be one of the most challenging parts of the design. For insights on how the wiring was routed from the aerial motors to the flight computer, see **Appendix J**.

Another important consideration was how the battery could be safely disconnected from the rest of the wiring in case of a malfunction while inaccessible inside a compartment that was sealed with cured silicone. To solve this problem, waterproof female and male XT60W connectors were run in and out of another hole in the top seal (see **Figure 4.20** and **Figure 4.25**). These were wired between the battery and the electronic speed controllers which allowed for the circuit to be disconnected externally. A convenient side effect of implementing this safety feature was the added ability to recharge the LiPo battery while it was sealed in the compartment. This was not possible before and required removing the cured silicone each time.

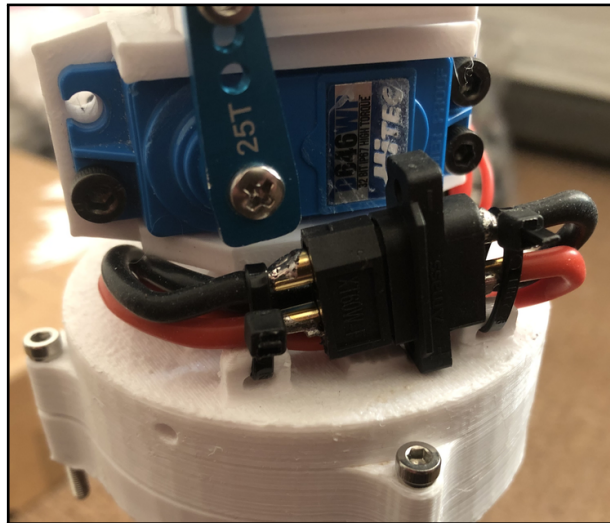


Figure 4.25: XT60W waterproof connectors outside the waterproof compartment to charge and disconnect the battery externally

### 4.4.1 Flight Computer

Since the primary focus of this project was not to design custom electrical components, a premade flight computer (FC) was purchased: the SpeedyBee F7 V3 (see **Figure 4.26**). This FC has the ability to flash custom-configured flight control software onto it through Bluetooth, which significantly simplified the flight control programming process. It also has an integrated inertial measurement unit (IMU) and barometer (altitude), which are sensors required to stabilize the vehicle during its hover.

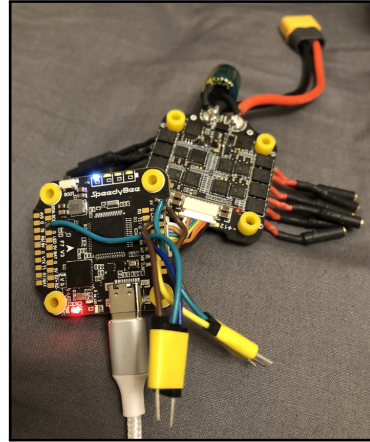


Figure 4.26: SpeedyBee F7 V3 BL32 50A 30x30 flight computer connected to a 4-in-1 ESC

#### 4.4.2 iNAV Firmware

To control all parts of the vehicle, from arming to aquatic ascent to aerial hovering, the iNAV 6 Horizon Hawk firmware package was used. This is a popular flight control software that allows quadcopters to be controlled and configured through a user-friendly interface. The primary reason for choosing this firmware was its support for customizable vehicle configurations with autonomous flight profiles. In iNAV, the user can set separate flight modes which are tied to the state of the vehicle. For instance, the vehicle could be configured to power the aquatic motor for a set amount of time and then switch to an existing iNAV mode called "position hold" whereby the vehicle would automatically attempt to maintain a fixed altitude and horizontal position in the air.

#### 4.4.3 PID Controller

Within the iNAV firmware, there exists an implementation of a simple proportional-integral-derivative (PID) controller which is often used for controlling quadcopters. This is a controller which takes in the angular positions of the vehicle and multiplies them by three separate gain values to correct the response of the motors toward a desired angle (see **Figure 4.27**). Each of these modifies a specific error response: P - proportional error; I - cumulative error; D - anticipatory error. These were each tuned within the iNAV firmware to ensure the vehicle would hover in a stable manner.

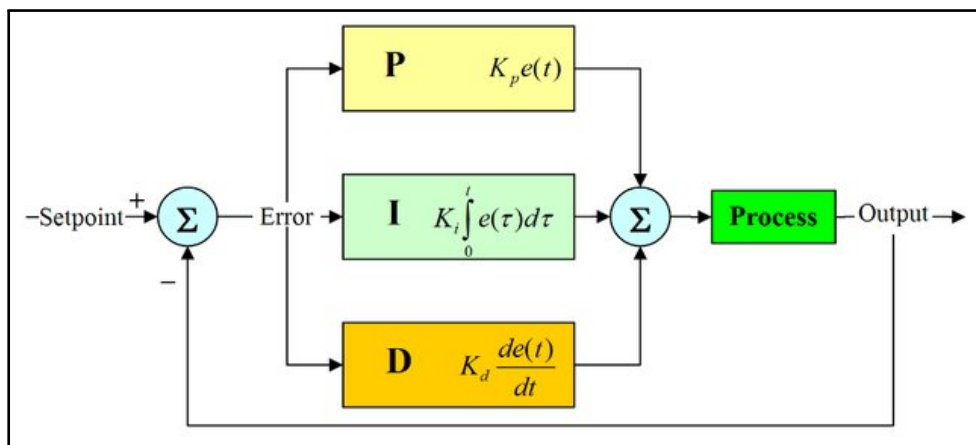


Figure 4.27: PID controller model used in this project [43]

#### 4.4.4 Communication Systems

Another significant challenge in the execution of this project was establishing communication with the vehicle while it was submerged in the water. This is because the conductive ions in unpurified water inhibit the propagation of radio waves. As a result, high-frequency (HF) radio waves are able to penetrate less than a meter of water [44]. This presented an issue due to the 2-meter depth of the FloWave pool. While the vehicle could be armed above the water and programmed to automatically begin the maneuver after a certain amount of time (using a timer), this would present a significant safety risk by not allowing an abort to be called after lowering it into the test pool. Therefore, to tackle this problem, various submarine communication systems were researched: sonar, optical lasers, and extremely low frequency (ELF) radio waves, among others. Each one had downsides from complexity to a requirement for long antennas. Instead, the simplest solution was to tether the vehicle to an HF radio receiver floating on a buoy on the surface of the water. This tether was both light and slack, which meant that it was unlikely to interfere with the vehicle's motion. The tether entered the waterproof compartment through a hole in the aquatic motor housing (see **Figure 4.28**).

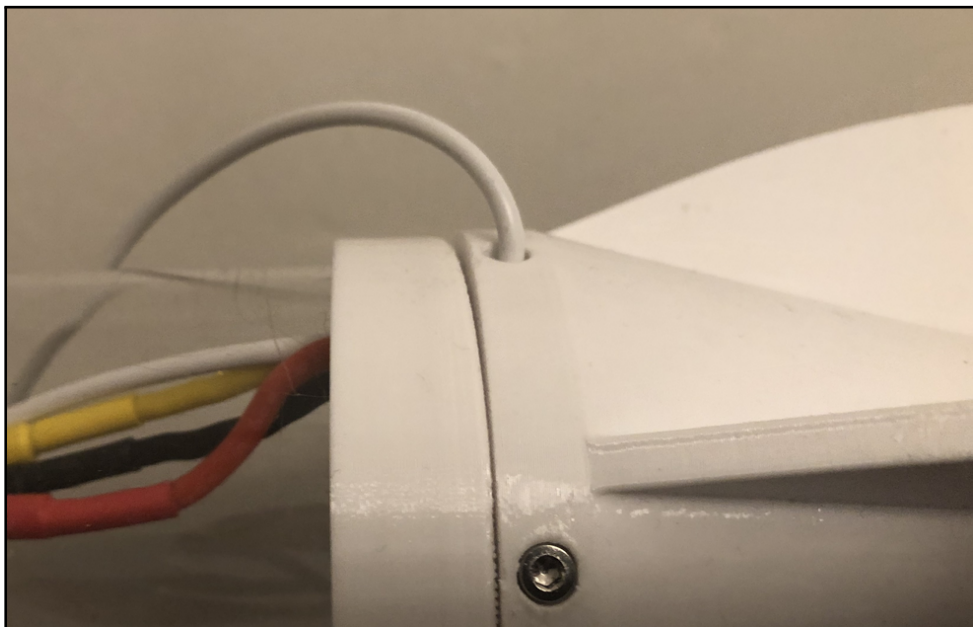


Figure 4.28: Hole in aquatic motor housing allows for receiver wire to run out of the vehicle to the floating buoy

#### 4.4.5 Signal Transmission

In order to send radio signals to the vehicle, the ExpressLRS (ELRS) protocol was chosen as it is an open-source radio protocol that works with inexpensive transmitter hardware while achieving high sensitivity and low latency (< 4 ms) [45]. For information regarding the transmitter and GPS choice, please see **Appendix K**.

# Chapter 5

## Manufacturing and Assembly

Seeing as an iterative design approach was used, the rapid manufacturing of redesigned components played a big role in the successful execution of the project. This section briefly illustrates all the means of fabrication and assembly which were utilized to achieve the final prototype vehicle.

### 5.1 Structural Elements

Most of the structural elements of the vehicle were fabricated using additive manufacturing (3D printing), more specifically fused deposition modeling (FDM). Past experience with this technique made it favorable compared to other machining methods. An Original Prusa MINI 3D printer was also readily available and was therefore used extensively throughout the project. One limitation of this printer, however, was its relatively small printing volume ( $18 \times 18 \times 18$  cm). This primarily constrained the size of the nose cone, which was 25 cm long, requiring it to be printed in two halves.

All of the 3D-printed structural components of the vehicle were manufactured out of polyethylene terephthalate glycol (PETG). This material was used due to its high water resistance, durability, and compatibility with the chosen 3D printer [46, 47].

The waterproof compartment was made from impact-resistant acrylic, which was cut to size with a hacksaw. This resulted in a very uneven cross section for the tube (see **Figure 5.1**). It was crucial to ensure that the end of the tube was as flat as possible because this would control the vertical alignment of the aquatic and aerial sections. Any misalignment could result in the vehicle biasing toward one direction during its ascent, likely making the maneuver unstable. A belt sander device was used to flatten the entire surface evenly and a spirit-level instrument to confirm it was horizontal to the ground.



Figure 5.1: Acrylic tubing roughness after cutting

## 5.2 Electronics Assembly

While the flight computer and ESCs were purchased from a supplier, they did require some assembly. Namely, bullet connectors were soldered onto the ESC terminals (see **Figure 1.2** and **Figure 4.26**) to allow for disconnecting the aerial motor wiring when changing structural elements. This was done using a soldering iron at the university's electronics laboratory. In the same location, a heat gun was used to contract heat-shrink tubing around the exposed wiring and attachments to prevent electrical short circuits from occurring. Afterward, a digital multimeter confirmed the continuity of these connections. Note that while some figures in this report may show exposed connections, all wiring was adequately protected with heat-shrink tubing before attaching to the battery.

## 5.3 Waterproofing Process

Before risking water damage to the sensitive electronics, the waterproofing method was tested on a separate identical water compartment to ensure it would prevent water from entering the compartment. Silicone sealant was applied all around the seams of the aquatic seals as well as in the holes through which the wires entered. The sealant was left untouched for 24 hours as noted on its instructions, after which it had cured fully and formed a strong mechanical bond between the acrylic tubing and PETG material (see **Figure 5.2**). The test piece was submerged in about 30 cm of water for only a few seconds and immediately showed some water entering the compartment through a small gap in the wiring hole seal. This test made it highly apparent that the waterproofing of the final assembly with all the electronics would have to be done rigorously and with careful preliminary testing to check that a proper seal had been formed before full submersion under water. After reapplying more sealant to the hole and repeating the test, no water entered the compartment.



Figure 5.2: Waterproofing test of 3D printed seals, left: seam; right: wire entry hole

## 5.4 Final Assembly

Once the integrity of the waterproofing process was confirmed, the vehicle could finally be fully assembled. The assembly process was simplified and sped up significantly by the abundance of soldered electrical connectors between the various components, allowing for the aerial and aquatic sections to be disconnected and built separately. See **Figure 5.3** and **Figure 5.4** below for the completed vehicle prototype.

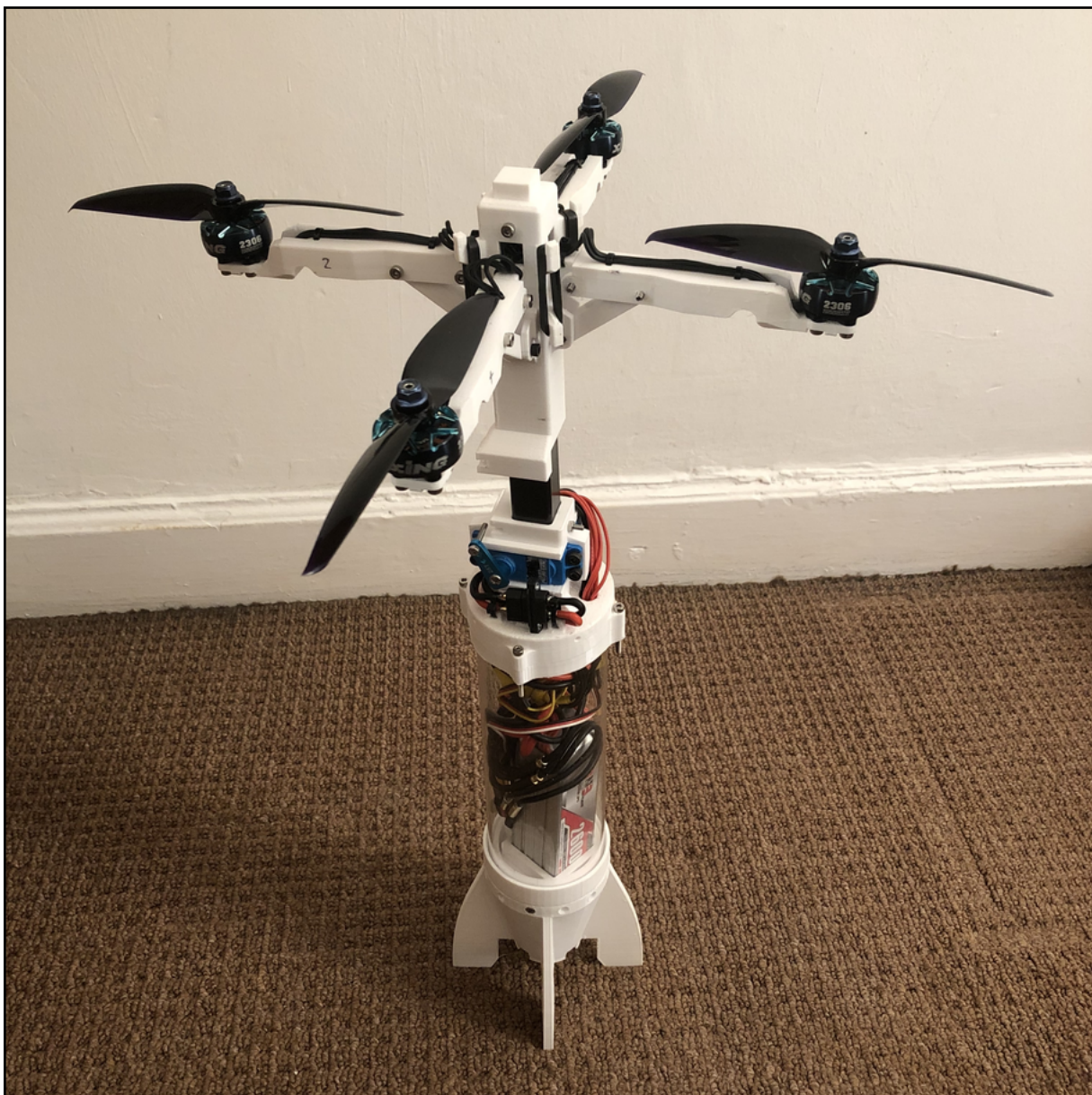


Figure 5.3: Final assembly of the aerial-aquatic vehicle with nose cone removed (open state)



Figure 5.4: Final assembly of the aerial-aquatic vehicle with nose cone (closed state)

# Chapter 6

## Experiments and Results

As part of testing whether or not the design could rapidly and successfully complete the water-to-air transition maneuver, this chapter aimed to evaluate how quickly the unfolding transition mechanism could open and to characterize the relationship between the force stored in the mechanism and its unfolding time. Knowing this is crucial to select the optimal number of rubber bands for the vehicle. While Hooke's law indicates the relationship to be linear, it is important to analyze the practical phenomena which may occur during the opening and assess whether or not more force is better. Before starting the primary experiment to examine this, the spring constant and hence elastic force exerted by the rubber bands on the unfolding mechanism had to be found. To do this, the extension and force of the rubber bands was measured and a simple Hookean relationship was formed. By taking multiple measurements at different extensions, the spring constant was found and could be used to figure out the force exerted by the rubber bands on the unfolding mechanism (since they were known to extend to 6 cm in the aquatic configuration). The force exerted by one rubber band (RB) was found to be equivalent to 3.8 N. This conversion can be used to generalize and compare the obtained results with any future unfolding UAAV systems that do not use rubber bands.

### 6.1 Unfolding Mechanism Opening Times

The second experiment aimed to measure the opening time of the unfolding mechanism and evaluate its translational behavior in the vertical direction. The experimental procedure is briefly described below:

1. The prototype vehicle was set vertically on top of a marker on the ground which would allow for the experiment to be conducted numerous times from the same reference point.
2. A camera capable of recording in slow motion (120 FPS) was attached to a fixed holder clamp and set to record the vehicle starting from the folded aquatic configuration.
3. A signal was sent to the servo to move the locking pin and allow for the mechanism to unfold into the aerial configuration.
4. The above step was repeated three times to obtain precise results after which the number of rubber bands on the hooks was increased starting from 4 to 6, 8, 10, 12, and 14. Four rubber bands were the minimum to provide sufficient force to open the mechanism fully.
5. The slow motion video was exported to the computer where the Kinovea software package was used to track the relative position of the aerial motor with respect to its starting point (see **Figure 6.1**).

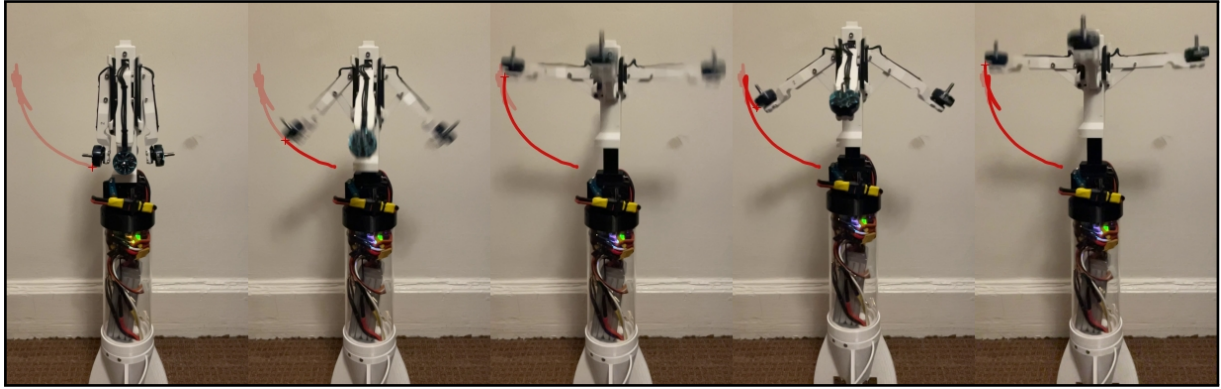


Figure 6.1: Consecutive snapshots showing Kinovea tracking the vertical position/velocity/acceleration of the aerial motor

The term RB will henceforth be used to refer to the trials conducted as part of the above experiment (e.g. "the 4 RB trial" in reference to the trial with four rubber bands). The data obtained in these two experiments are presented below.

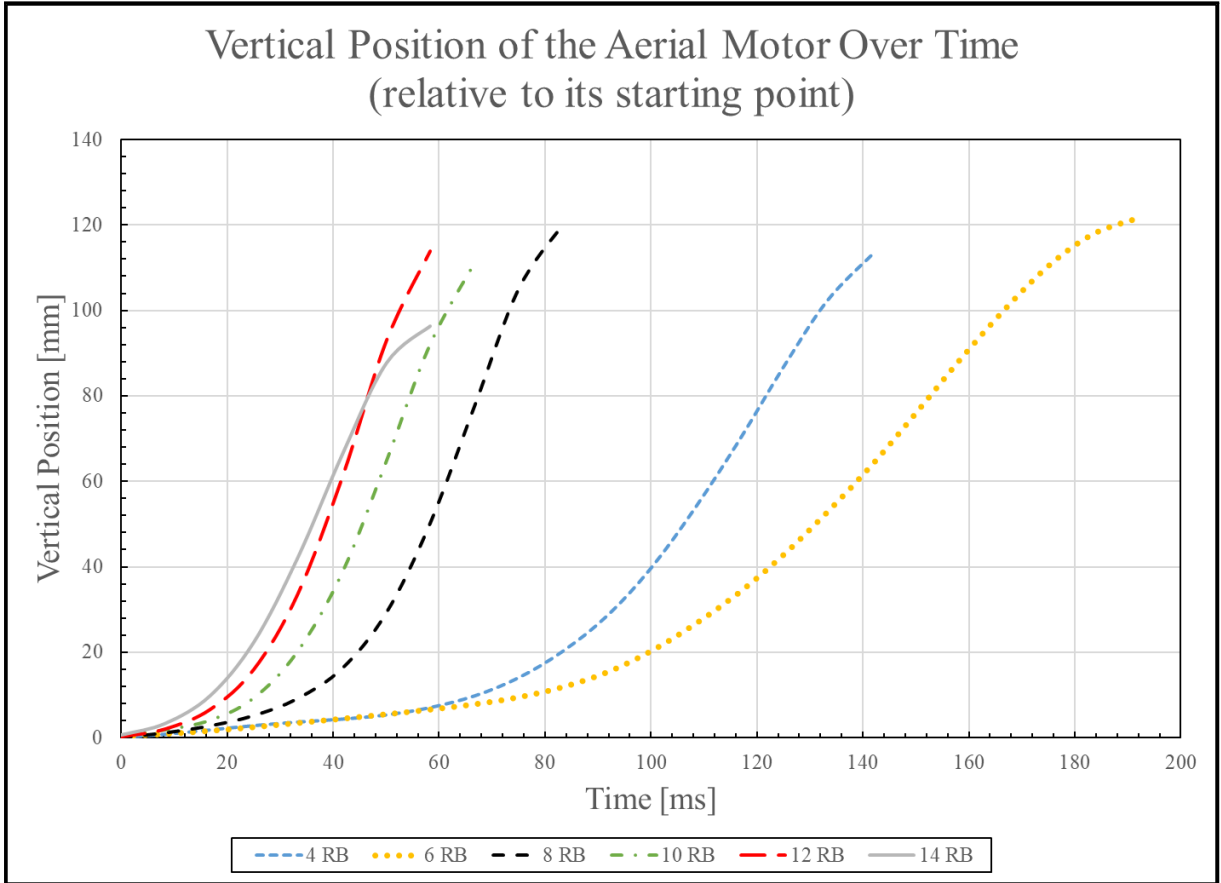


Figure 6.2: Relationship between the vertical position of the aerial motor and the time after the release of the unfolding mechanism

**Figure 6.2** contains each RB trial from the start of movement of the aerial motor to when it reaches its peak vertical position. The oscillations which follow have been cut off for clarity. Due

to slight variations in the vehicle's position from one trial to the next, all of the figures have been normalized to an initial position/velocity/acceleration of zero. The results in **Figure 6.2** show that, on average, increasing the number of rubber bands (RB) (i.e. the elastic force in the system) leads to a faster peak vertical position of the aerial motor. This is evidenced by the fact that the curves trend toward the left as RB increases. One exception to this is the case of 6 RB, which has the slowest time to peak (192 ms). It should be noted that 4 RB and 6 RB follow the same path for much longer than the rest of the curves. All of the curves have slightly varying peak vertical positions because the entire vehicle underwent a vertical acceleration due to the impact of the frame arm with the top runner (see **Figure 4.4** and **Figure D.1**). However, 14 RB has a peak prominently lower than the rest of the trials. Notably, it also has the fastest time to peak (58 ms).

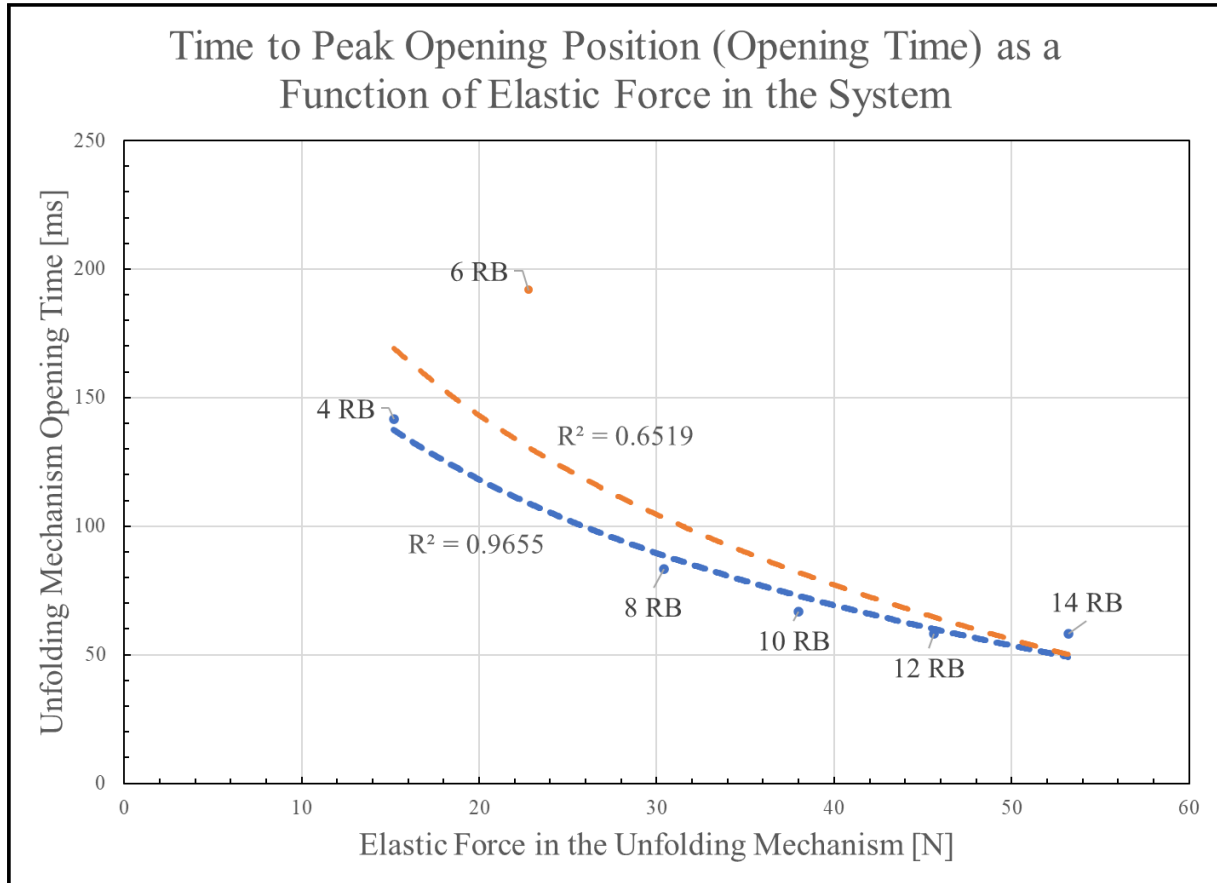


Figure 6.3: Relationship between the elastic force on the unfolding mechanism and its opening time

**Figure 6.3** was created by taking the time to peak of each trial from **Figure 6.2** and graphing it against the force equivalent of each corresponding trial RB. The best-fit trend line follows a logarithmic decay with an R-squared (good-of-fit) value of 0.65. If 6 RB is removed, this increases to 0.97, which likely indicates an anomaly in that trial run.

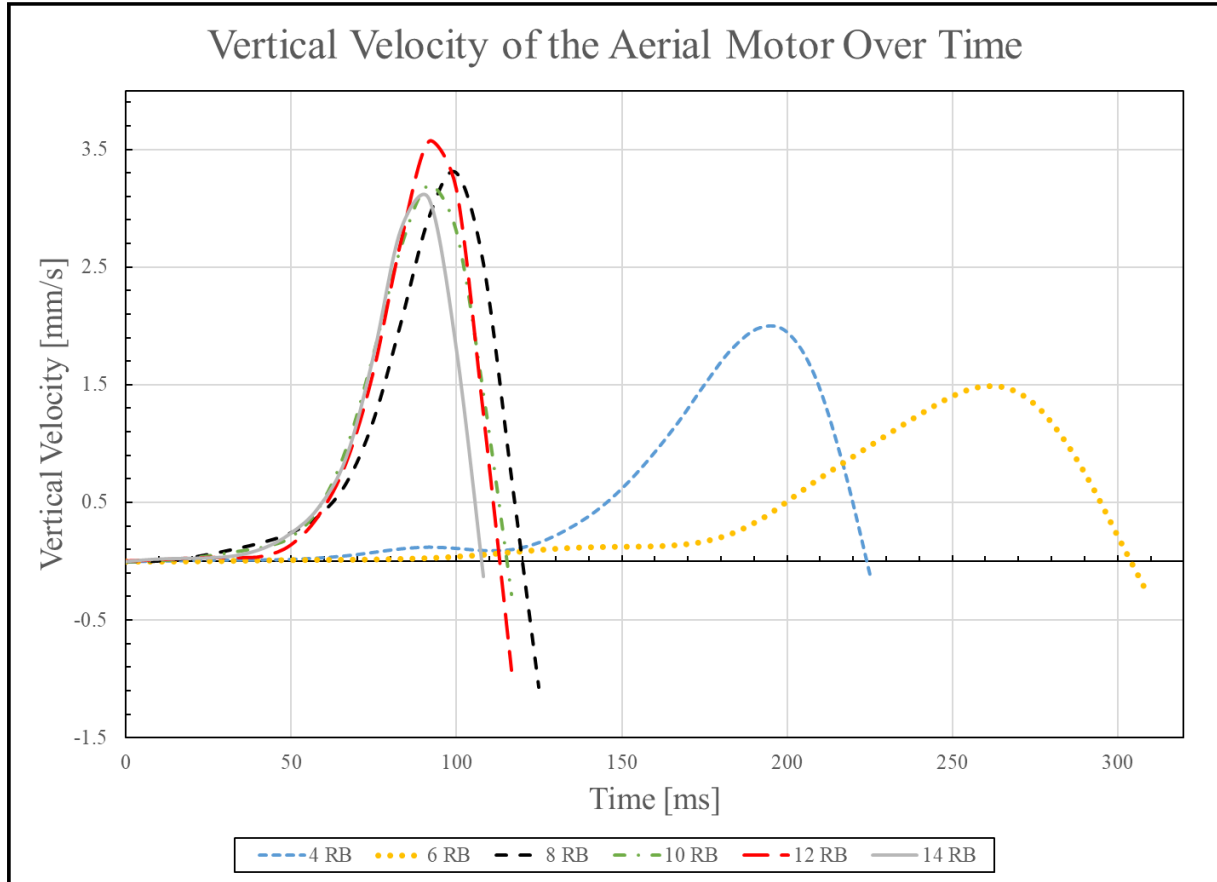


Figure 6.4: Relationship between the vertical velocity of the aerial motor and the time after the release of the unfolding mechanism

**Figure 6.4** highlights the vertical velocity curves of the trials. Each curve shows a steep positive slope, which occurs when the servo releases the bottom runner, and a sharp drop in velocity (to zero) when the bottom runner collides with the top runner and the mechanism momentarily stops moving. This is why the curves are cut off at the first value after crossing the x-axis, which is the peak vertical position of the aerial motor (i.e. the peaks in **Figure 6.2**). These cut-off points differ for each curve due to the abrupt velocity changes at higher rubber band counts with no change in sampling rate. Similar to the position curves, the velocities trend toward the left as RB increases, with 6 RB again being an exception. 4 RB also shows a small local peak in velocity (0.12 mm/s) at 92 ms. At the same point in time, 12 RB shows the highest vertical velocity of all the trials (3.57 mm/s).

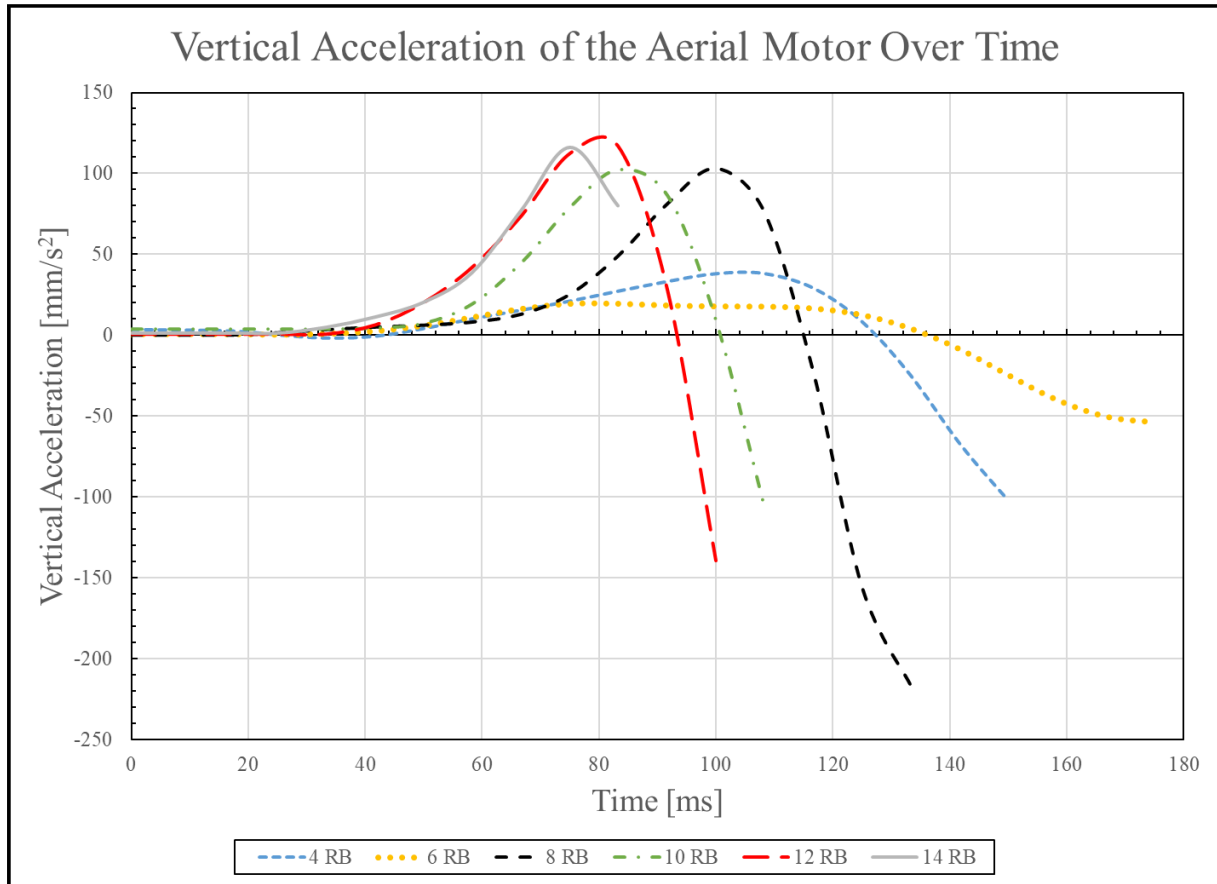


Figure 6.5: Relationship between the vertical acceleration of the aerial motor and the time after the release of the unfolding mechanism

In **Figure 6.5**, vertical acceleration for the course of each trial is displayed. Of note is the more dramatic difference observed between the low and high RB trials, with the 4 and 6 RB curves flattening. As before, data is only presented until the peak vertical position (i.e. when the bottom runner is at its highest acceleration in the negative direction and beginning oscillations). However, 14 RB does not reach a negative acceleration at all.

# Chapter 7

## Discussion

### 7.1 Experimental Outcomes

The peak vertical position and force versus opening time graphs clearly showed that the mechanism unfolds quicker as the number of rubber bands increased. The reason for this is that the added elastic force of the rubber bands increases the acceleration of the bottom runner and hence frame arms, leading to a faster unfolding time, as was expected. All of the peak vertical positions were within a standard deviation of 8 mm from the mean, which decreased to 4 mm if disregarding the 14 RB trial. This is an acceptable deviation given the limitations of the experimental apparatus (see **Section 7.1.1**). The reasoning for discounting 14 RB in this calculation was due to a large amount of frame arm protrusion at such a high rubber band count causing the aerial motors to start from a higher relative vertical position compared to, for instance, the 4 RB trial. Since the data in the position graph was normalized so that the tracking software would assume the coordinate system to start on the tracking point, the 14 RB trial reached a seemingly lower vertical peak position compared to other trials when in reality it simply had to travel a shorter distance to the peak (see **Figure 7.1**).

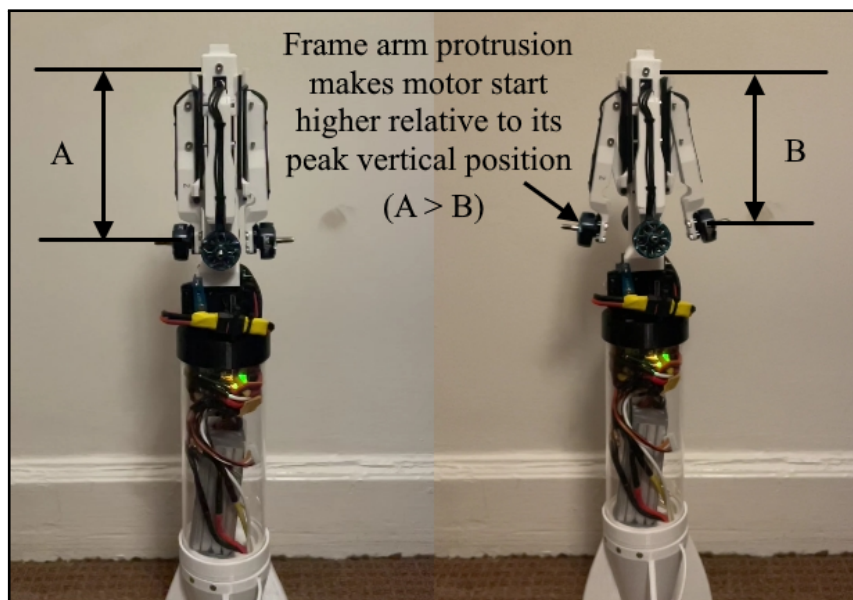


Figure 7.1: The influence of high rubber band count on the vertical starting position. Left: 4 RB; Right: 14 RB

One peculiar detail in the vertical position graph was the delayed vertical peak of 6 RB. Both the 4 and 6 RB trials follow the same curve until about 58 ms after which they deviate, which indicates that below a certain rubber band count, the unfolding mechanism may behave differently, leading to a delayed release of the bottom runner.

The velocity results confirmed this suspicion. The same pattern followed: a higher RB meant a higher initial velocity, aside from 4 and 6 RB, where the velocity peaks were not only lower than the other trials but also occurred later. Notably, there was a small local vertical velocity maximum in the 4 RB trial, indicating that a momentary oscillation or disturbance occurred before releasing the bottom runner. This strongly suggested that the method of releasing these trials had a systematic error present.

The acceleration graph gave insights into the possible source of this error as it showed the other trials to have a regular-shaped acceleration whereas the 4 and 6 RB trials had significantly flattened positive acceleration peaks. This flattening effect pointed toward a loss of potential energy from the elastic rubber bands directly after release, meaning the servo locking pin was likely getting stuck on the runner cutout for longer than the other trials resulting in a lower initial positive acceleration. A further indication of this was that the 6 RB trial had two acceleration maximums before the first minimum, which is consistent with the runner being released and getting caught on, something momentarily decreasing its acceleration.

Aside from this, the acceleration graph also showed a clear convergence of curves toward the 14 RB trial line. While increasing the rubber band count from 8 to 10 shifted the acceleration peak to the left by 17 ms, going from 12 to 14 rubber bands only shifted the peak by 8 ms, indicating a slowing trend in the impulse of the mechanism while still increasing the maximum positive acceleration. This means that while 12 and 14 RB may have the same opening time (see **Figure 6.2** peaks), 14 RB will result in a larger force between the two runners when colliding. Since the design did not include a damping mechanism, this impulse force increase led to a fracture in the bottom runner when a trial was attempted with 16 rubber bands. The ideal force condition was therefore found to be such that the acceleration curves converge while having as low maximum acceleration as possible to reduce the likelihood of fracture or excessive oscillations. If undamped, these oscillations could lead to controllability issues when attempting the maneuver. In combination with the logarithmic decay shown in the force versus opening time graph, which is consistent with an asymptote existing at low forces (infinite opening time due to insufficient force), this result shows that there is an optimal opening time that can be achieved while keeping stresses on the system components at a minimum. In the particular case of this unfolding mechanism, that optimal time was achieved with 12 rubber bands, which is equivalent to 45.6 N of elastic force.

### 7.1.1 Sources of Error and Limitations

Perhaps the largest source of error in these experiments was caused by the fact that the vehicle was not fixed to the ground while conducting the data collection. This meant that the vehicle would accelerate vertically upward directly after the servo was released due to the elastic energy stored in the rubber bands (see **Figure 7.2**). These vertical accelerations were likely the primary cause of discrepancies in the peak vertical positions seen in **Figure 6.2**, for instance when comparing the 8 and 10 RB trials.

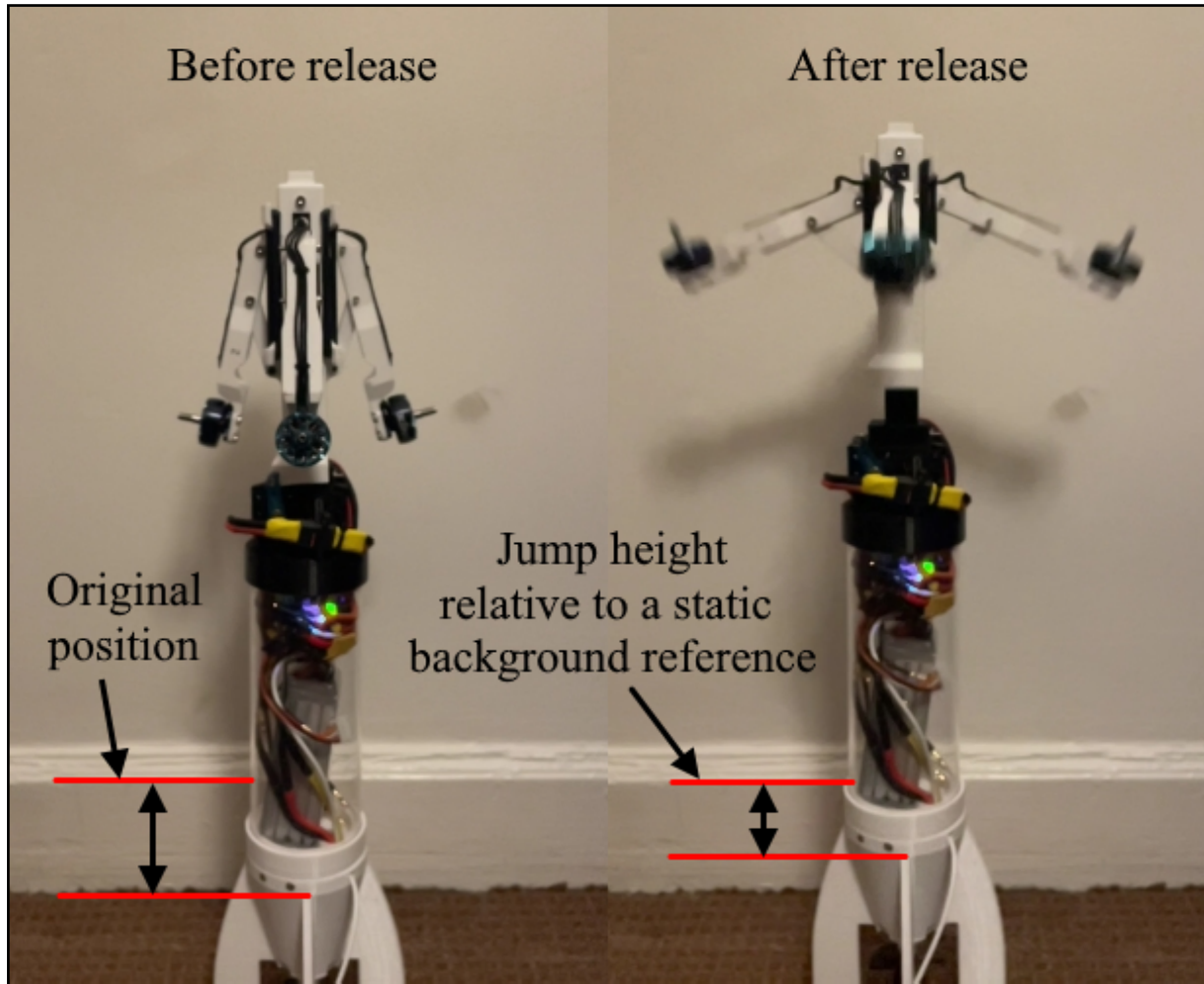


Figure 7.2: A significant vertical offset 58 ms after releasing the servo during the 14 RB trial

Given the findings discussed in **Section 7.1**, it is highly likely that the servo used in the release mechanism introduced a unique error phenomenon that only affected the lower rubber band count trials. While analyzing the slow motion footage from the 4 and 6 RB trials, it became apparent that the servo did not fully move out of the way when it began its motion (see **Figure 7.3**). The bottom runner began to slowly slide upward but got momentarily stuck on the locking bolt, which could have led to the significant decrease in peak accelerations as seen in **Figure 6.5**, due to losing some of the rubber bands' elastic energy.

The servo pin was released by manually moving a slider from 1500 to 0, which may mean that human error caused this phenomenon to occur. It is hypothesized that the reason this phenomenon did not occur in the larger rubber band count trials was that they had sufficient force to quickly slide past the servo locking pin, whereas the lower rubber band counts may have gotten slowed slightly due to not exerting enough force to push the pin away.

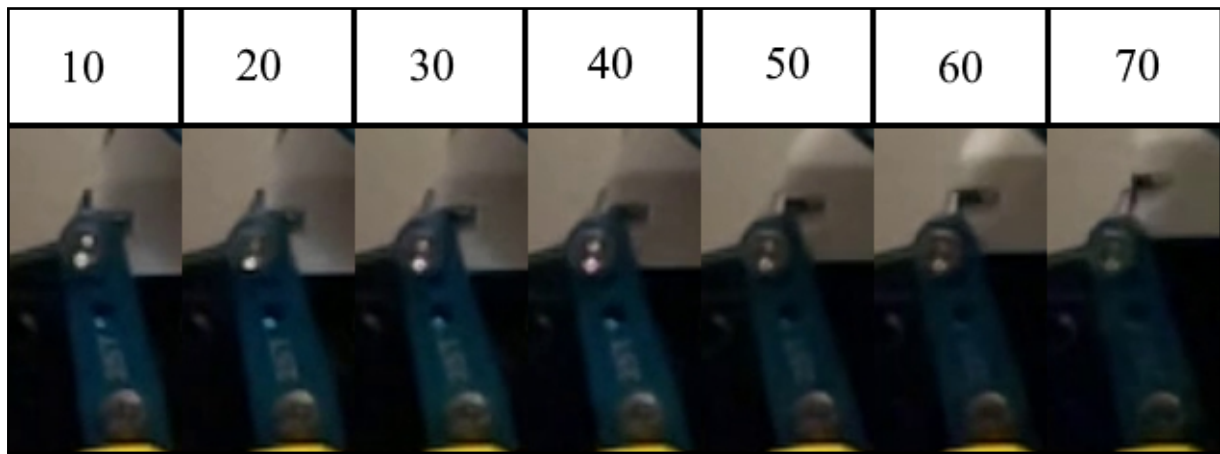


Figure 7.3: A frame-by-frame magnification (milliseconds since release indicated on top) showing the servo locking pin hugging the bottom runner during the 40-60 ms times (4 RB trial)

Lastly, a factor that led to significant limitations in the precision of data was the relatively low frame rate camera used for recording the slow-motion footage for the experiment. The available camera equipment was only capable of recording 120 FPS, which allowed the videos to be slowed by four times the regular speed, resulting in a minimum time step of only about 8.3 ms. This led to the tracking software not being able to follow the full path of the aerial motor for high rubber band counts where the large acceleration led to significant position jumps between frames. In some cases, such as in the 14 RB trial, this resulted in the software losing track of the aerial motor's vertical position and cutting the data collection short. This is most visible in **Figure 6.5** where the 14 RB curve stops early before decelerating. This limitation may also be a partial cause for the lower peak vertical position of the 14 RB trial in **Figure 6.2**.

### 7.1.2 Experimental Improvements

In order to improve the precision and accuracy of the experiment in the future, the following suggestions should be considered:

- Normalizing the vertical position data around the peak height instead of the aerial motor position in the aquatic configuration would allow for a fair of time to peak without being influenced by the protrusion of the frame arms. Alternatively, the protrusion could be eliminated by redesigning the runner release mechanism.
- Mounting the vehicle to the ground before conducting future experiments would prevent it from jumping into the air and influencing the vertical offset obtained by the tracking software.
- The tracking capabilities and accuracy of the software could be improved by making the backdrop of the test a checked pattern and adding high-contrast tracking markers onto the vehicle instead of using the corner of the aerial motor.
- Higher frame rate slow-motion camera equipment would allow for improved resolution which would increase the precision of tracking high acceleration trials.
- A different approach to tracking the vehicle could be pursued, for instance using more accurate motion sensors instead of a camera.

- More trials could be conducted, especially at both extremes of rubber band counts. This could give further insights into the issue with the servo locking pin.
- A foam pad could be added below the top runner to dampen any oscillations and get more accurate peak results by reducing the vibration of the system after impact.

## 7.2 Success Aspects

Since a successful and rapid water-to-air transition was determined to be a key aspect of proving the viability of this vehicle, the experiments in this project primarily focused on characterizing this part of the maneuver by determining the optimal force needed to open the mechanism rapidly while putting as little stress on the vehicle as possible to avoid fracture. The conducted experiments provided many insights into the practical nuances of the unfolding mechanism as well as generalizing the obtained findings to mechanisms that may utilize other force systems (springs, leadscrews, etc) via the conversion of RB to Newtons. As a practical engineering project, this thesis produced a prototype vehicle that is currently capable of the following feats:

1. Protecting all the sensitive electronics through waterproofing (see **Figure 5.2** and **Appendix G**).
2. Being charged and disconnected with external waterproof connectors while sealed (see **Figure 4.25**).
3. Lowering itself into the testing pool via a hook on the nose cone (see **Figure F.2**).
4. Establishing radio communication to a programmed transmitter through a floating radio antenna (see **Figure 4.28**).
5. Receiving an arming command to power on the aquatic motor (see **Appendix L.1**).
6. Maintaining a folded aquatic configuration throughout an aquatic ascent (see **Figure 5.4**).
7. Unfolding itself into an aerial configuration in a matter of about 58 milliseconds (see **Appendix L.3** and **Appendix L.4**).
8. Powering on the aerial motors (see **Appendix L.2**).

## 7.3 Future Opportunities

If desired (or given a lengthier project timeline), more experiments could be conducted to fully characterize all aspects of the vehicle. First and foremost the aquatic motor thrust could be tested by submerging it in a tank of water and measuring the force on a strain gauge. This would experimentally confirm that the aquatic propeller choice is powerful enough to lift the 2 kg vehicle out of the water with sufficient acceleration for it to remain airborne and unfold itself. Secondly, the stability of the transition maneuver could be characterized by recording slow-motion footage of the vehicle unfolding and immediately activating its aerial motor to see if the vehicle could handle the oscillations and impulse force caused by the rubber bands. These two experiments would significantly strengthen the confidence that the constructed vehicle can indeed complete each individual stage of motion required for the full water-to-air maneuver.

# **Chapter 8**

## **Conclusion**

In conclusion, this project achieved its primary goal of designing and manufacturing C.U.R.I.C.O, the hybrid aerial-aquatic vehicle. In the process, many insights were gained into the nuanced design process behind every component and system of the vehicle. The revelations and pitfalls of the iterative design process were thoroughly documented to aid future researchers in gaining knowledge about the many complex subsystems of such a vehicle. It also presented results to support the choice of an optimal amount of force to open the unfolding mechanism in the least amount of time. This knowledge can be applied to similar prototypes in the future. The allocated timeline for the project was from January 16th until April 26th (100 days). This limited amount of available time placed a constraint on the number of design iterations and conceptual changes which could be made. What remains is to tune the controllability of the vehicle to achieve stable flight. After that is done, it is ready to be taken to the FloWave testing facility where it can attempt the water-to-air transition maneuver. Based on the 58 millisecond time to transition from an aquatic configuration to an aerial one, it seems highly probable that the vehicle will have sufficient time to unfold itself rapidly and attempt stable flight while still airborne. Whether or not the aquatic portion of the maneuver is vertically stable remains to be seen through further experimentation and iteration. While this project may already be seen as a success by some given the limited time available, the testing steps are still ahead.

# References

- [1] F. Nex, C. Armenakis, M. Cramer, D.A. Cucci, M. Gerke, E. Honkavaara, A. Kukko, C. Persello, and J. Skaloud. Uav in the advent of the twenties: Where we stand and what is next. *ISPRS Journal of Photogrammetry and Remote Sensing*, 184:215–242, 2022. ISSN 0924-2716. doi: <https://doi.org/10.1016/j.isprsjprs.2021.12.006>. URL <https://www.sciencedirect.com/science/article/pii/S0924271621003282>.
- [2] Brian P. Tice. Unmanned aerial vehicles – the force multiplier of the 1990s. *Airpower Journal*, Spring 1991. URL <https://web.archive.org/web/20090724015052/http://www.airpower.maxwell.af.mil/airchronicles/apj/apj91/spr91/4spr91.htm>.
- [3] Ed Alvarado. 237 ways drone applications revolutionize business. *Drone Industry Insights*, 5 2021. URL <https://droneii.com/237-ways-drone-applications-revolutionize-business>.
- [4] John W. R. Taylor. *Jane's Pocket Book of Remotely Piloted Vehicles*. Collier Books, 1977.
- [5] J.M. Sullivan. Evolution or revolution? the rise of uavs. *IEEE Technology and Society Magazine*, 25(3):43–49, 2006. doi: 10.1109/MTAS.2006.1700021.
- [6] J. C. Mohanta & Pankaj Singh Yadav Faiyaz Ahmed. Recent advances in unmanned aerial vehicles: A review. *Arab J Sci Eng*, 47, 2022. doi: 10.1007/s13369-022-06738-0.
- [7] Fintan Corrigan. How a quadcopter works along with propellers and motors, 2020. URL <https://www.dronezon.com/learn-about-drones-quadcopters/how-a-quadcopter-works-with-propellers-and-motors-direction-design-explained/>.
- [8] Dan Mototolea. A study on the actual and upcoming drone communication systems. In *2019 International Symposium on Signals, Circuits and Systems (ISSCS)*, pages 1–4, 2019. doi: 10.1109/ISSCS.2019.8801800.
- [9] Kai Li, Ning Lu, Pei Zhang, Wei Ni, and Eduardo Tovar. Poster abstract: Multi-drone assisted internet of things testbed based on bluetooth 5 communications. In *2020 19th ACM/IEEE International Conference on Information Processing in Sensor Networks (IPSN)*, pages 345–346, 2020. doi: 10.1109/IPSN48710.2020.00-14.
- [10] Jarrod C Hodgson, Shane M Baylis, Rowan Mott, Ashley Herrod, and Rohan H Clarke. Precision wildlife monitoring using unmanned aerial vehicles. *Scientific reports*, 6(1):1–7, 2016.
- [11] Ahmad Hashim and Mohamad Tamizi. Development of drone for search and rescue operation in malaysia flood disaster. *International Journal of Engineering & Technology*, 7:9, 07 2018. doi: 10.14419/ijet.v7i3.7.16195.

- [12] Antoine Gademer, Florent Mainfroy, Laurent Beaudoin, Loïca Avantey, Vincent Germain, Corentin Chéron, Sébastien Monat, and Jean-Paul Rudant. Solutions for near real time cartography from a mini-quadrotor uav. *Proc SPIE*, 7478, 09 2009. doi: 10.1117/12.830391.
- [13] Yuly Peristiowati, Novita Anggraeni, Aladdin Purkuncoro, and Hariyono Hariyono. Dji phantom frame quadcopter for aerial monitoring of objects: A preliminary study of quadcopter design for natural disaster detection. *International journal of health sciences*, 6:1565–1578, 10 2022. doi: 10.53730/ijhs.v6n3.13265.
- [14] Salimzhan A. Gafurov and Evgeniy V. Klochkov. Autonomous unmanned underwater vehicles development tendencies. *Procedia Engineering*, 106:141–148, 2015. ISSN 1877-7058. doi: <https://doi.org/10.1016/j.proeng.2015.06.017>. URL <https://www.sciencedirect.com/science/article/pii/S187770581500942X>. Proceedings of the 2nd International Conference on Dynamics and Vibroacoustics of Machines (DVM2014) September 15 –17, 2014 Samara, Russia.
- [15] Andrew Tarantola. This rov dives 2,000 feet to save sailors on a sunken submarine. *Gizmodo*, 10 2012. URL <https://gizmodo.com/this-rov-dives-2-000-feet-to-save-sailors-on-a-sunken-s-5950700>.
- [16] National Research Council. Undersea vehicles and national needs. *The National Academies Press*, 1996. doi: 10.17226/5069.
- [17] Brian C. Juskiewicz John P. Friedman. Submarine rescue the past, present, and future of deep submergence rescue. *U.S. Naval Institute*, 2020. URL <https://www.usni.org/magazines/proceedings/2020/october/submarine-rescue>.
- [18] National Sun Yat sen University. The basic components of an rov. *Institute of Undersea Technology*, 2016. URL <http://www.iut.nsysu.edu.tw/hhchen/html/underwatertech/rovch3.pdf>.
- [19] WHOI. Slocum glider. *Woods Hole Oceanographic Institution*, 2023. URL <https://www.whoi.edu/what-we-do/explore/underwater-vehicles/auvs/slocum-glider/>.
- [20] Liam Paull, Sajad Saeedi, Mae Seto, and Howard Li. Auv navigation and localization: A review. *IEEE Journal of Oceanic Engineering*, 39(1):131–149, 2014. doi: 10.1109/JOE.2013.2278891.
- [21] Qiu Suming and Cui Weicheng. An overview on aquatic unmanned aerial vehicles. *Annual Review of Materials Research*, 11 2019. doi: 10.19080/ARR.2019.05.555663. URL <https://juniperpublishers.com/arr/pdf/ARR.MS.ID.555663.pdf>.
- [22] Diego A. Mercado, Marco M. Maia, and F. Javier Diez. Aerial-underwater systems, a new paradigm in unmanned vehicles. In *2017 International Conference on Unmanned Aircraft Systems (ICUAS)*, pages 1690–1695, 2017. doi: 10.1109/ICUAS.2017.7991362.
- [23] C. Genaro Carreon, C. Oliver M. Huerta, M. Alfredo Arias, C. Sergio Torres, and José Ángel L. Ortega H. Amphibious propeller optimization for aerial and underwater operation. In Eusebio E. Hernandez, Sajjad Keshtkar, and S. Ivvan Valdez, editors, *Industrial and Robotic Systems*, pages 85–96, Cham, 2020. Springer International Publishing. ISBN 978-3-030-45402-9.
- [24] Lei Li, Siqi Wang, Yiyuan Zhang, Shanyuan Song, Chuqian Wang, Shaochang Tan, Wei Zhao, Gang Wang, Wenguang Sun, Fuqiang Yang, Jiaqi Liu, Bohan Chen, Haoyuan Xu, Pham Nguyen,

- Mirko Kovac, and Li Wen. Aerial-aquatic robots capable of crossing the air-water boundary and hitchhiking on surfaces. *Science Robotics*, 7(66):eabm6695, 2022. doi: 10.1126/scirobotics.abm6695. URL <https://www.science.org/doi/abs/10.1126/scirobotics.abm6695>.
- [25] John Davenport. How and why do flying fish fly? *Reviews in Fish Biology and Fisheries*, 4(2):184–214, Jun 1994. ISSN 1573-5184. doi: 10.1007/BF00044128. URL <https://doi.org/10.1007/BF00044128>.
- [26] Yufeng Chen, Hongqiang Wang, E. Farrell Helbling, Noah T. Jafferis, Raphael Zufferey, Aaron Ong, Kevin Ma, Nicholas Gravish, Pakpong Chirarattananon, Mirko Kovac, and Robert J. Wood. A biologically inspired, flapping-wing, hybrid aerial-aquatic microrobot. *Science Robotics*, 2(11):eaa05619, 2017. doi: 10.1126/scirobotics.eaa05619. URL <https://www.science.org/doi/abs/10.1126/scirobotics.eaa05619>.
- [27] Stefano Mintchev and Dario Floreano. Adaptive morphology: A design principle for multimodal and multifunctional robots. *IEEE Robotics & Automation Magazine*, 23:42–54, 09 2016. doi: 10.1109/MRA.2016.2580593.
- [28] R Siddall and M Kovač. Launching the aquamav: bioinspired design for aerial–aquatic robotic platforms. *Bioinspiration & Biomimetics*, 9(3):031001, mar 2014. doi: 10.1088/1748-3182/9/3/031001. URL <https://dx.doi.org/10.1088/1748-3182/9/3/031001>.
- [29] Marco M. Maia, Diego A. Mercado, and F. Javier Diez. Design and implementation of multirotor aerial-underwater vehicles with experimental results. In *2017 IEEE/RSJ International Conference on Intelligent Robots and Systems (IROS)*, pages 961–966, 2017. doi: 10.1109/IROS.2017.8202261.
- [30] Warren Weisler, William Stewart, Mark B. Anderson, Kara J. Peters, Ashok Gopalarathnam, and Matthew Bryant. Testing and characterization of a fixed wing cross-domain unmanned vehicle operating in aerial and underwater environments. *IEEE Journal of Oceanic Engineering*, 43(4):969–982, 2018. doi: 10.1109/JOE.2017.2742798.
- [31] Oscar Liang. How to choose fpv drone motors, March 2023. URL <https://oscarliang.com/motors/>.
- [32] Hartzell Propeller. Are more propeller blades better?, 2018. URL <https://hartzellprop.com/are-more-propeller-blades-better/>.
- [33] Oscar Liang. Lookup table: Motor & prop sizes, kv, lipo cell count, and weight for fpv drone builds, March 2021. URL <https://oscarliang.com/table-prop-motor-lipo-weight/>.
- [34] Jyotishkumar Parameswaranpillai, C.D. Midhun Dominic, Sanjay Mavinkere Rangappa, Suchart Siengchin, and Togay Ozbaakkaloglu. 1 - introduction to elastomers. In Sanjay Mavinkere Rangappa, Jyotishkumar Parameswaranpillai, Suchart Siengchin, and Togay Ozbaakkaloglu, editors, *Elastomer Blends and Composites*, pages 1–9. Elsevier, 2022. ISBN 978-0-323-85832-8. doi: <https://doi.org/10.1016/B978-0-323-85832-8.00002-X>. URL <https://www.sciencedirect.com/science/article/pii/B978032385832800002X>.
- [35] Mercury Marine. Prop blade rake: Not easy to explain, but crucial for optimal boating, September 2020. URL <https://www.mercurymarine.com/en/us/dockline/prop-blade-rake-not-easy-to-explain-but-crucial-for-optimal-boating>.

- [36] Anthony F. Molland, Stephen R. Turnock, and Dominic A. Hudson. *Propeller Characteristics*, page 277–312. Cambridge University Press, 2 edition, 2017. doi: 10.1017/9781316494196.014.
- [37] Paul Cooper. Angry shark pro 6s turnigy xk3674 2200kv 40mm 1.9p prop, September 2019. URL <https://www.youtube.com/watch?v=7CpHPCgn6o>.
- [38] Aditya Rajan. A review on nose cone designs for different flight regimes. *International Research Journal of Engineering and Technology*, August 2020. URL <https://www.irjet.net/archives/V7/I8/IRJET-V7I8605.pdf>.
- [39] F l a n k e r. Nose cone general dimensions, May 2009.
- [40] IanSan5653. Nose cone design, July 2018.
- [41] iFlight. Xing2 2306 4s 6s fpv motor, 2021. URL <https://shop.iflight-rc.com/xing2-2306-4s-6s-fpv-motor-unibell-pro1465>.
- [42] HobbyKing. Turnigy xk3674-2200kv 1750w brushless inrunner, February 2023. URL [https://hobbyking.com/en\\_us/turnigy-xk3674-2200kv-1750w-brushless-inrunner.html](https://hobbyking.com/en_us/turnigy-xk3674-2200kv-1750w-brushless-inrunner.html).
- [43] Arrak M. Edan. An optimized pid parameters for lfc in interconnected power systems using msl optimization algorithm. *ARPJ Journal of Engineering and Applied Sciences*, 10 2016.
- [44] Umair Mujtaba et al Qureshi. Rf path and absorption loss estimation for underwater wireless sensor networks in different water environments. *National Library of Medicine*, June 2016. URL <https://www.ncbi.nlm.nih.gov/pmc/articles/PMC4934316/>.
- [45] ExpressLRS. High-performance open source radio control link, January 2023. URL <https://www.expresslrs.org>.
- [46] Petg characteristics. <https://dielectricmfg.com/resources/knowledge-base/petg/>, 2019. Accessed: 2023-04-22.
- [47] Daniel Moreno Nieto, Maria Alonso García, Miguel Angel Vicente, and Lucia rodriguez parada. Product design by additive manufacturing for water environments: Study of degradation and absorption behavior of pla and petg. *Polymers*, 13:1036, 03 2021. doi: 10.3390/polym13071036.
- [48] Ben Winstanley. Brushed dc motors vs. brushless dc motors, July 2020. URL <https://www.haredataelectronics.co.uk/brushed-dc-motors-vs-brushless-dc-motors>.
- [49] Carbon fiber pultrusions. <https://media.easycomposites.co.uk/datasheets/EC-TDS-Carbon-Fibre-Pultrusions.pdf>, 2023. Accessed: 2023-04-22.
- [50] What is the density of stainless steel? <https://www.kloecknermetals.com/blog/what-is-the-density-of-stainless-steel/>, 2021. Accessed: 2023-04-22.
- [51] Enhanced shotbolt solenoid lock. <https://www.hazardexonthenet.net/article/34490/Enhanced-shotbolt-solenoid-lock.aspx>, 2010. Accessed: 2023-04-22.
- [52] Marcel J. Sidi. *Single- and Dual-Spin Stabilization*, page 132–151. Cambridge Aerospace Series. Cambridge University Press, 1997. doi: 10.1017/CBO9780511815652.007.
- [53] HobbyRC. Gnb 2600mah 4s 120c lipo battery, January 2023. URL <https://www.hobbyrc.co.uk/gnb-2600mah-4s-120c-lipo-battery>.



## Appendix A

# Project Plan

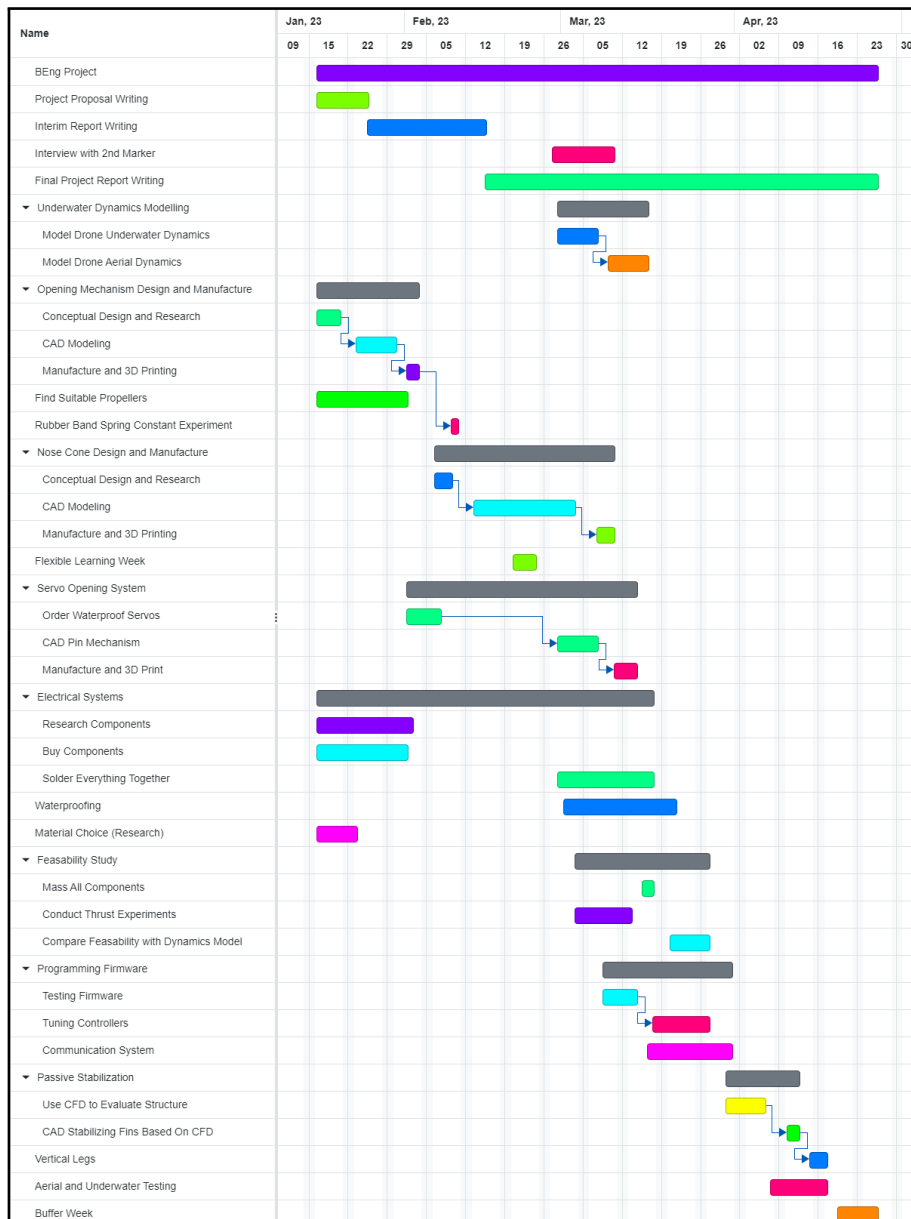


Figure A.1: Complete Gantt chart plan for the thesis project



## Appendix B

# Risk Register

Table B.1: Risk Register

Risk Identification			Risk Assessment			Risk Control	
Date	Category	Risk Description	Probability (1-5)	Consequence (1-5)	Severity (Priority)	Mitigation	Contingency Plan
23/01/2023	Hardware	Purchased components not arriving on time	2	4	High	Order things with a safety factor of time in advance	If the components do not arrive on time, find alternative components from faster suppliers
23/01/2023	Hardware	Component failure under water	4	2	Low	Testing the water proofing before inserting the electrical components in it	Purchase new components and address cause of water leak
23/01/2023	Facility	Testing facility (FloWave) not available	3	3	Medium	Book FloWave facility well ahead of any testing needs	Use an alternative facility at Heriot-Watt University through supervisor contact
23/01/2023	Practical	Water-exit maneuver is not vertical	3	2	Low	Add passive stabilization to the vehicle in the form of fins and low center of gravity	Tune aerial PID controllers to respond to a non-vertical water-exit (angled)
23/01/2023	Practical	Project does not reach intended milestones on time	3	3	Medium	Gantt Chart, planning things well in advance, starting the project early, and making progress through iterative design	Report on the data that was able to be collected and highlight the successful parts of the projects
23/01/2023	Practical	Vehicle does not have sufficient thrust to perform the maneuver	2	5	High	Establish a theoretical dynamic model of the vehicle underwater to check required thrust and measure motor outputs in static thrust tests	Add additional underwater motors to the vehicle (design with this in mind) and upgrade aerial motors if necessary

# Appendix C

## Motors

### C.1 Brushed versus Brushless Motor Choice

The first step in selecting a motor was the choice of motor type: brushed or brushless. Brushed motors tend to wear out quicker due to the brushes being in contact with the commutator (see **Figure C.1**). For the same reason, brushed motors have more energy losses due to friction and heat. As the budget did not significantly restrict it, the more expensive and durable brushless motors were chosen due to their superior efficiency and power [48].

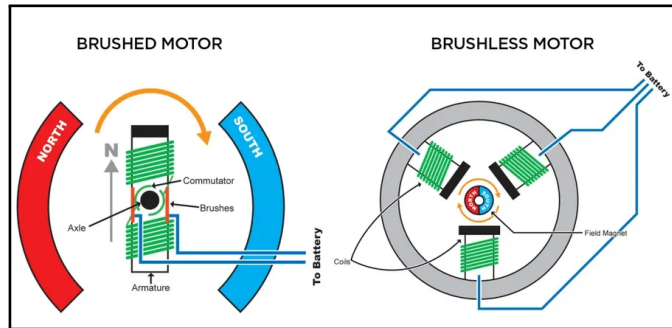


Figure C.1: Comparison of brushless and brushed motor configurations [48]

### C.2 Aquatic Motor Choice

There were some initial considerations to use the same motor for aerial and aquatic maneuvering with a custom propeller design which would unfold when the density of the medium changed. The concern with this approach, however, was whether or not the aerial motors could create sufficient vertical thrust to lift the entire vehicle while folded and pointing horizontally outward. As such, the arms which held the motors would have to be angled outward (see **Figure C.2**), creating more drag on the vehicle which would slow it during its ascent, defeating the purpose of creating a rapidly transitioning vehicle. Since the motion constraints placed on the vehicle only required a short vertical ascent during the aquatic phase, the decision was made to mount a separate more powerful aquatic motor on the bottom of the vehicle and add passive stabilization tail fins to help control its attitude.

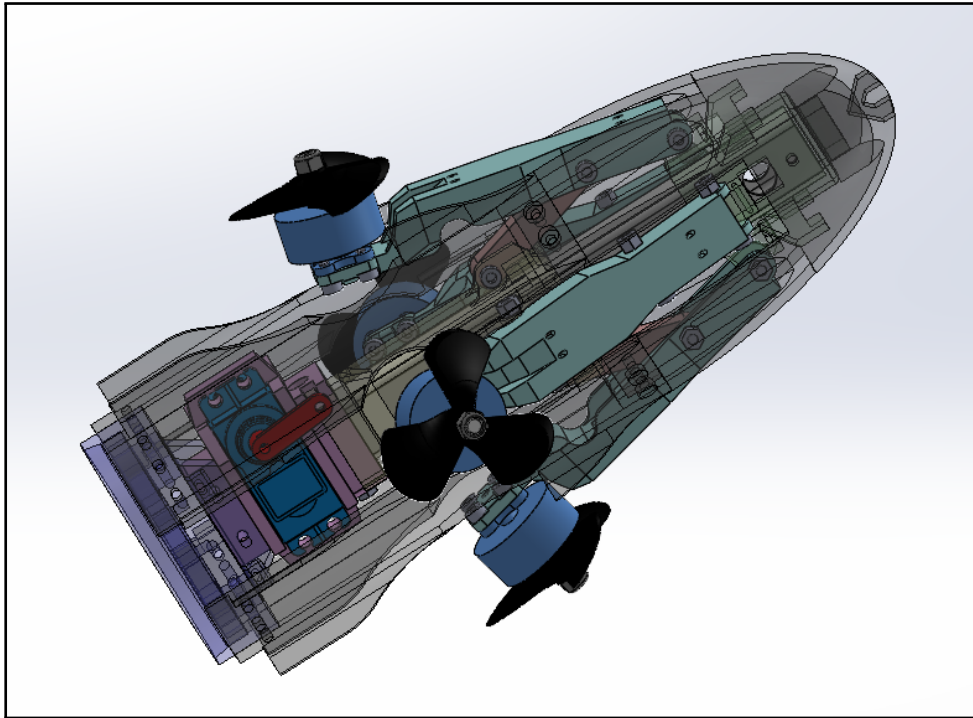


Figure C.2: Hybrid motor approach would increase drag on the vehicle due to protrusion of frame arms in order to produce vertical thrust

It was estimated that the chosen bare motor (see **Figure C.3**) could achieve a maximum rotation speed of up to 37,000 RPM (this of course would be lowered significantly with the propeller attached). Having such a large rotation speed meant that while the motor was likely overspecified for its use case, the chosen configuration could be tested with different propellers if the chosen one did not produce sufficient thrust to lift the vehicle. Due to the time constraints of the thesis and the inexpensive nature of aquatic propellers, the iterative trial and error approach would be used to settle on a propeller.



Figure C.3: Motor and propeller combination: Turnigy XK3674-2200KV 1750w Brushless Inrunner and TFL 56mm 3 Blade Nylon Propeller 10.75" Pitch (5mm) [42]

In order to turn the underwater motor off at an appropriate moment, a timer would be used which started counting from the beginning of the maneuver until the vehicle broke through the

water surface. By measuring the time it took for this to happen through multiple tests in the FloWave pool, this timing could be determined and programmed into the flight computer in order to complete the next stages of the transition maneuver (unfolding the vehicle and turning the aerial motors on). If the timeline of the project permitted, a sensor-based approach could have been explored, whereby a pressure sensor would detect the moment at which the vehicle exits the water, and automatically triggers the unfolding mechanism (and turns off the underwater motors).

Since the chosen motor was waterproof, it did not need to be coated with sealant. To mount it to the vehicle, bolts were used alongside a cutout in the aquatic seals to hold the motor firmly in place. Due to it being an inrunner motor, its outer housing did not spin. The propeller was attached to the motor shaft using a simple grub screw and a fastening bolt (see **Figure C.4**).

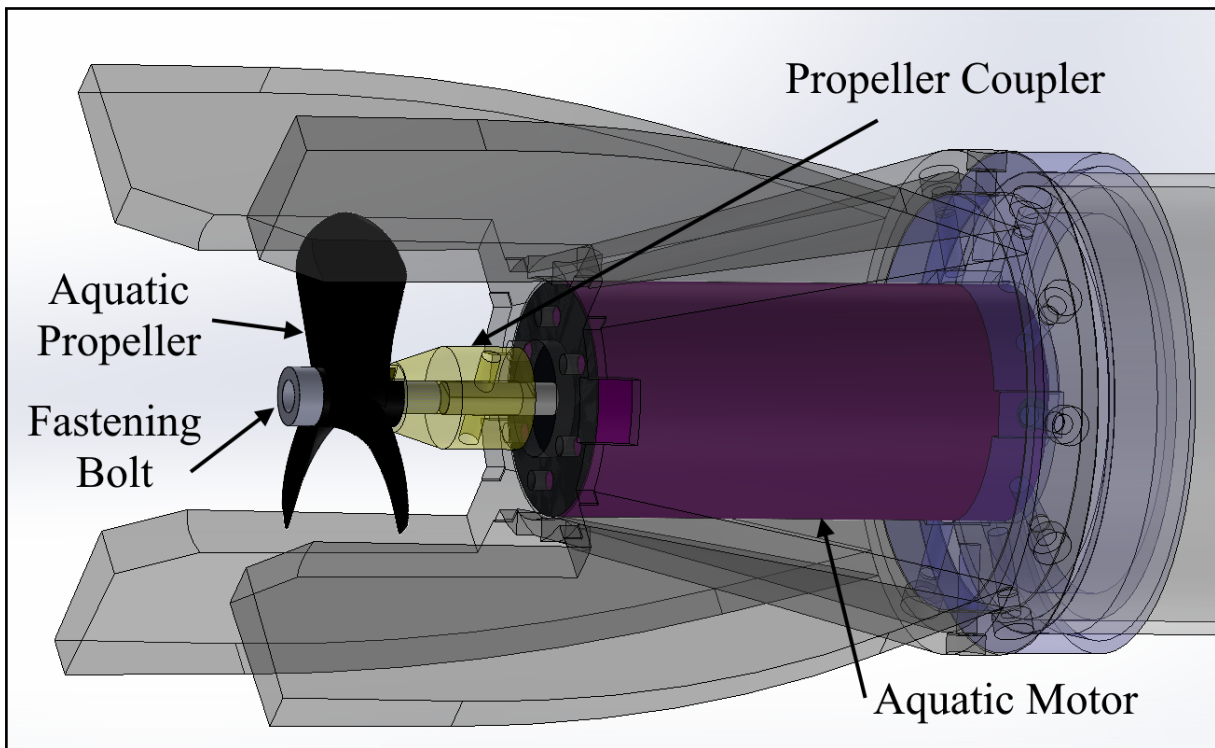


Figure C.4: Different parts of the aquatic propulsion system

### C.3 Aerial Motor Datasheet

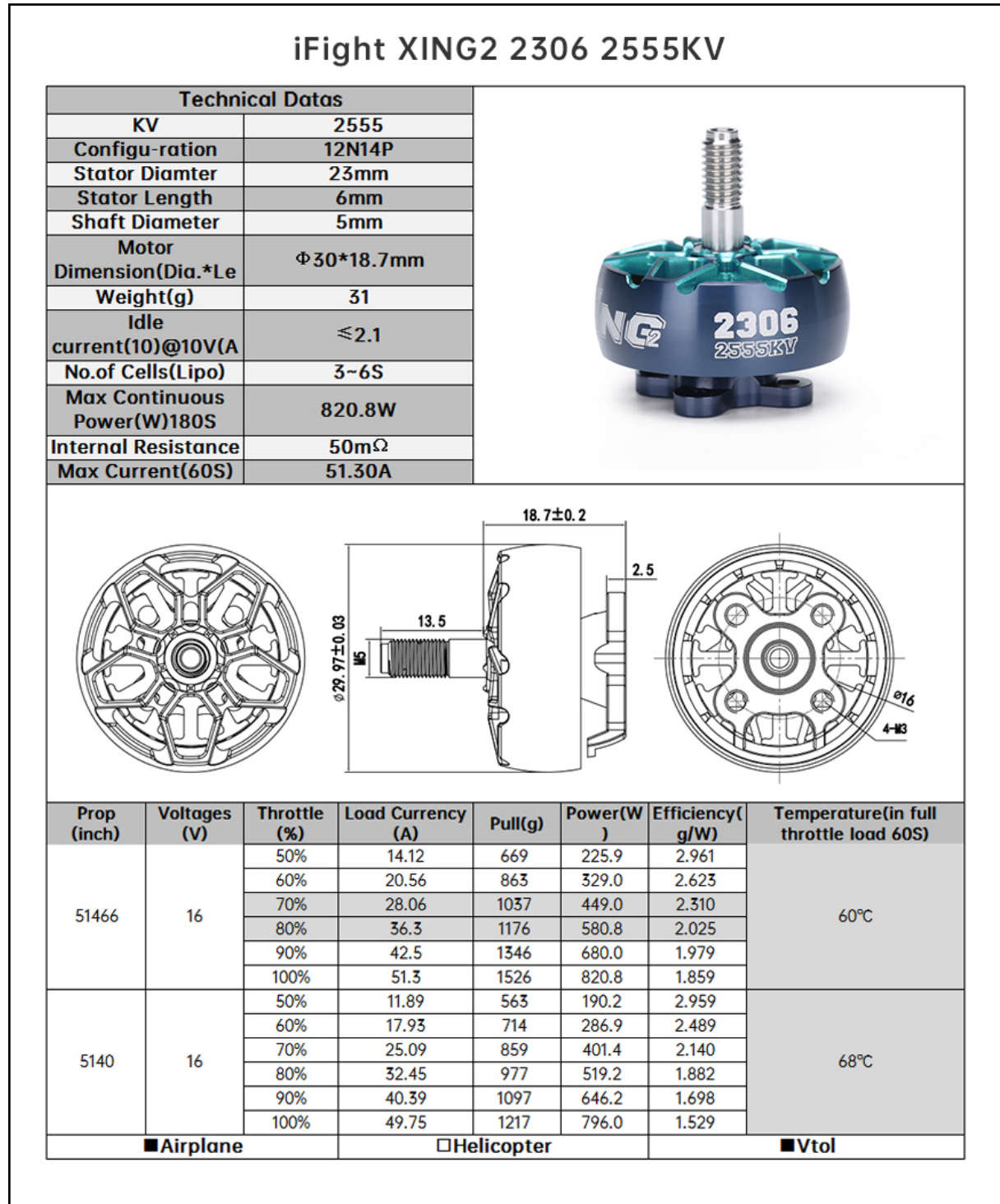


Figure C.5: Datasheet for the chosen aerial motor containing thrust estimates [41]

## Appendix D

# Unfolding Mechanism

Notably, one key issue that became apparent after manufacturing the first iteration of the unfolding mechanism was that moving the bottom runner would sometimes cause the mechanism to lock in place instead of opening as expected. This was because the top and bottom runner holes were aligned vertically. The tension force from the rubber bands pulled the runner arm into a locked position, creating a state of bistability, whereby the mechanism would not have any horizontal force to push it open. By shifting the bottom runner hole closer to its center, a horizontal force component was introduced which made the mechanism unstable and would lead to an automatic release upon allowing the bottom runner to move freely.

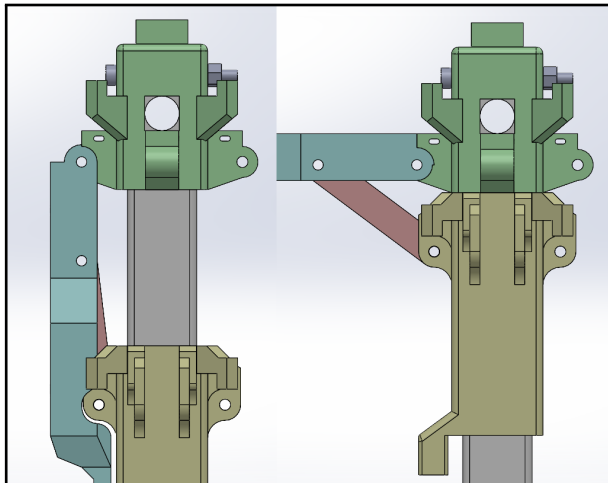


Figure D.1: Improved unfolding mechanism geometry without bistability

The choice of carbon fiber as the central shaft material was twofold. Firstly, carbon fiber is lightweight (approximately  $1.4 \text{ g/cm}^3$  [49]) which was crucial to keep the weight of the vehicle as low as possible. Secondly, it has favorable mechanical properties compared to plastic. Given the unfolding mechanism would undergo hundreds of openings during testing, it was crucial that the central shaft would be able to absorb and transfer the impact loads from the bottom runner crashing into the top runner (see **Figure D.2**).

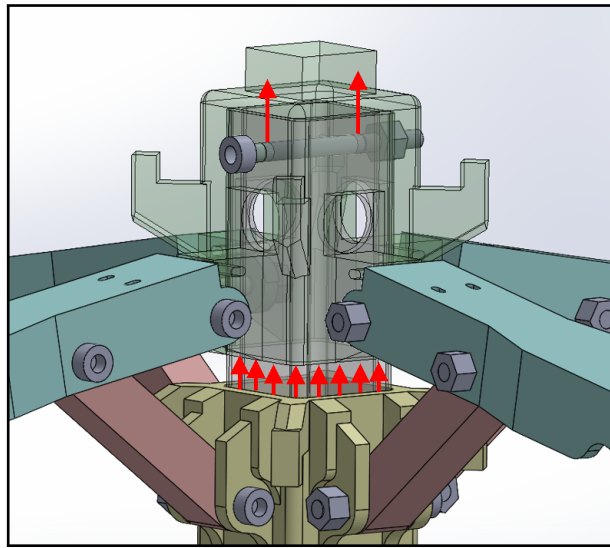


Figure D.2: The force of the two runners colliding is transferred into the central shaft via the mounting bolt

In order to absorb these forces without deforming, the chosen material had to be stiff. The Young's Modulus of carbon fiber is 34 GPa [49], as compared to 2 GPa for polyethylene terephthalate glycol (PETG) [46], a common plastic used in additive manufacturing. Using an alternative material such as steel would have made the shaft almost six times as heavy (the density of steel is about  $7.85 \text{ g/cm}^3$  [50]). Additionally, a hollow central shaft was chosen to allow for running the motor wires down to the flight computer (described further in **Section 4.4**).

## Appendix E

### Solenoid

Initially, the use of a solenoid lock release mechanism was considered for the release mechanism. These electromagnetic devices involve moving a pin back and forth through a locking channel using an electrical current in a coil (see **Figure E.1**).

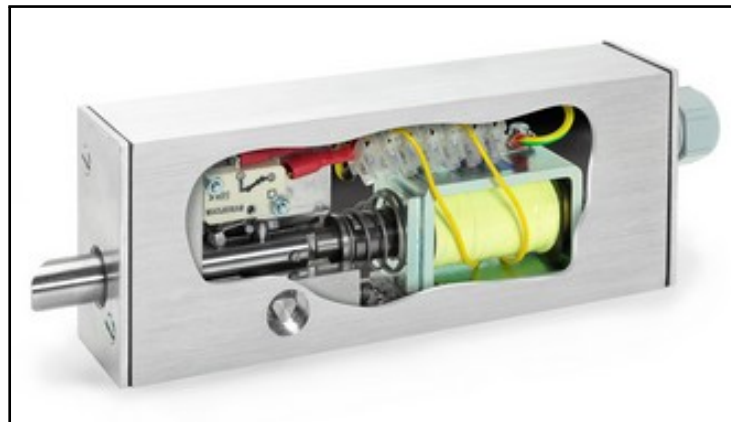


Figure E.1: Inner workings of a simple solenoid pin locking device [51]

If the bottom runner had a hole, the solenoid pin could keep the runner fixed in place until a release command was sent, after which the pin would move out of the hole, allowing the runner to move vertically upward from the tension of the rubber bands. There were, however, several drawbacks to using these locks which ultimately made them unsuitable for this design. Firstly, due to the linear push-pull motion of the pin, the solenoid lock would have to be mounted on the side of the central shaft, pointed toward it, which meant that the diameter of the vehicle would increase significantly in a single direction. This increase was undesirable as the vehicle would experience more drag underwater due to a larger cross-sectional area. Secondly, most readily available solenoid locks are not designed to work under a significant perpendicular force (i.e. the locking pin would be pulled upward by the rubber bands), which meant that the solenoid was unlikely to have enough torque to overcome the normal force between the locking pin and the runner hole.

## Appendix F

### Nose Cone

After determining the shape of the nose cone, it had to be modified to allow for the unfolding mechanism to deploy. This meant making rectangular cuts into the elliptical shape which matched the path swept by the frame arms and motor while opening (see **Figure 4.16**).

A downside of this requirement was that it exposed more of the opening mechanism to the flow of water, especially the aerial propellers, which increased the drag on the vehicle. In future designs, this could be avoided by using a diaphragm (similar to the ones found in camera apertures) which would improve streamlining during the aquatic ascent and open right before deployment of the unfolding mechanism.

The nose cone design was separated into pieces which made it possible to manufacture with 3D printers that have a smaller bed size, such as the one used throughout this project. As an additional benefit, this design decision made it possible to replace separate pieces of the nose cone in case of fracture and enabled the simple switching of the top nose cone shape if an alternative was desired. Lastly, a V-shaped cutout was added to the top of the nose cone to allow for the vehicle to be lowered to the bottom of the testing pool and released (see **Figure F.1**).

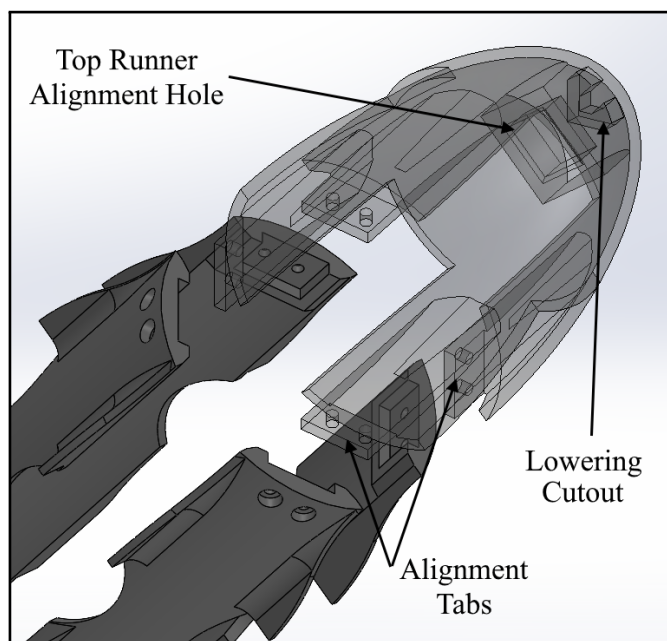


Figure F.1: Separated nose cone pieces and labeled design intricacies



Figure F.2: Proof of being able to lower the vehicle by a wire through the top cutout in the nose cone

## Appendix G

# Waterproofing

The seals were 3D printed out of PETG, a plastic material with high water resistance and good mechanical properties [47]. To ensure no water entered through the seals themselves, they were printed with 100% infill and a 0.15 mm layer height, which made them impermeable to water (confirmed through testing). Other than protecting the electronics from water, the seals also acted as structural frame elements which connected the aerial and aquatic sections together while also allowing for the flight computer to be mounted in alignment with the horizontal plane of the vehicle and for wiring to run into the compartment (see **Figure 4.20**).

In order to close the seam between the acrylic tubing and the seals, two options were considered: O-rings and silicone sealant. While O-rings are a common method of preventing liquids or gases from entering or escaping pressurized vessels, a lack of time made coating the seams with silicone sealant a more viable option for this project. Silicone sealant was also cured to provide a strong mechanical bond between the acrylic tubing and the seals, which removed the need for fastening them together with bolts. Despite using sealant, the design can be easily modified to utilize O-rings in the future by widening the space in which the acrylic tube slides into (see **Figure 4.20**).



Figure G.1: Waterproofing on final vehicle

## Appendix H

# Stabilization and Tail Fins

The center of pressure is the point on a vehicle where the sum of the pressure field can be considered to be acting as a force. If the center of pressure is ahead of the center of gravity (relative to the direction of travel), the vehicle will tend to try and reorient itself such that the center of gravity is in front. It is also likely that any misalignment between the center of thrust and center of mass would cause the vehicle to tilt in a certain direction. This means that in order for the vehicle to remain vertical and stable during its aquatic ascent stage, it must either implement an active stabilization system (such as having multiple motors with thrust throttling or a thrust vector control gimbal) or lower its center of pressure below the center of gravity.

The unidirectional torque created by the aquatic motor causes the vehicle to roll (due to the conservation of angular momentum). While counter-intuitive, this roll actually aids in further stabilizing the vehicle because of spin stabilization [52]. The principle behind this is that if the vehicle is spinning around its longitudinal (vertical) axis at a constant rate, a pitch in any direction will be shortly counteracted in the opposite direction due to the roll of the vehicle.

## Appendix I

# Battery and ESCs

### I.1 Battery

Two possible ways of powering the electronics and motors were explored. Firstly, the use of a tether was considered as it would remove the requirement for onboard power, which would reduce the weight of the vehicle by around 15% and shorten its vertical height by about 20%. The concern with this approach was that creating a tether with sufficiently low gauge wire may result in quite a heavy cable. Without an active stabilization system, this unbalanced weight may have been too significant for the vehicle to overcome on its own, leading to an attitude pitch during the aquatic ascent stage. It is also important to note that a tether would not eliminate the requirement for an onboard waterproof electronics compartment (as the flight computer needs to be attached to the frame for a stable hover), which meant that both aspects (tether and waterproofing) would need to be figured out instead of just one.

To estimate the maximum current output of the battery, **Equation (I.1)** was used:

$$I = C_r E_r \quad (I.1)$$

Where  $C_r$  is the current discharge rating ( $\text{hr}^{-1}$ ),  $E_r$  is the rated energy stored (Ah), and  $I$  is the continuous discharge current of the battery (A).

To power all four aerial motors at peak current, the battery would need to be capable of discharging 200A. The chosen 4S GNB LiPo battery has a discharge rating of 110C and a rated energy storage of 2600mAh [53], which gives a continuous current output of 286A, enough to power all aerial and aquatic motor(s) at the same time if required. The minimum flight time  $t$  of the vehicle was found to be about 47 seconds at a continuous 200A current (using **Equation (I.2)** below), which was deemed sufficient for demonstrating a stable hover after completing the transition maneuver.

$$t = \frac{E_r}{I} \quad (I.2)$$

While there were some attempts at designing housing for the battery and aquatic electronic speed controller (see **Figure I.1**), it was ultimately found to be unnecessary as the wiring and electronics were packed very tightly into the waterproof compartment which made it unlikely for anything to move during the maneuver (see **Figure 4.23**).

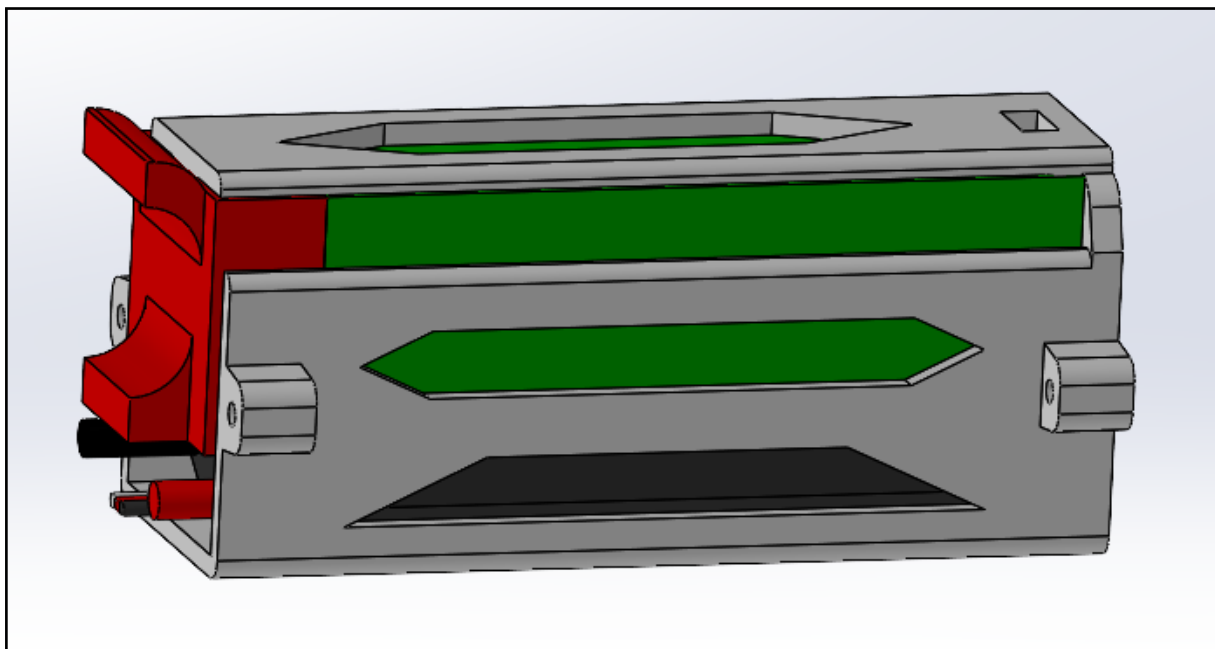


Figure I.1: Initial battery and electronic speed controller housing design

## I.2 Power Distribution

To regulate its speed, each motor needed an electronic speed controller (ESC). For the aerial motors, a 4-in-1 ESC power distribution board was used, which had a terminal for each individual motor. The aquatic motor required a separate larger ESC due to its higher current draw (see **Figure I.2**). These ESCs were wired to the battery with a parallel XT60 connector (see **Figure I.3**), since they would be powered at separate times without overlap.



Figure I.2: ESCs, left: SpeedyBee BL32 50A 4-in-1 ESC; right: Hobbywing Skywalker 80A UBEC ESC

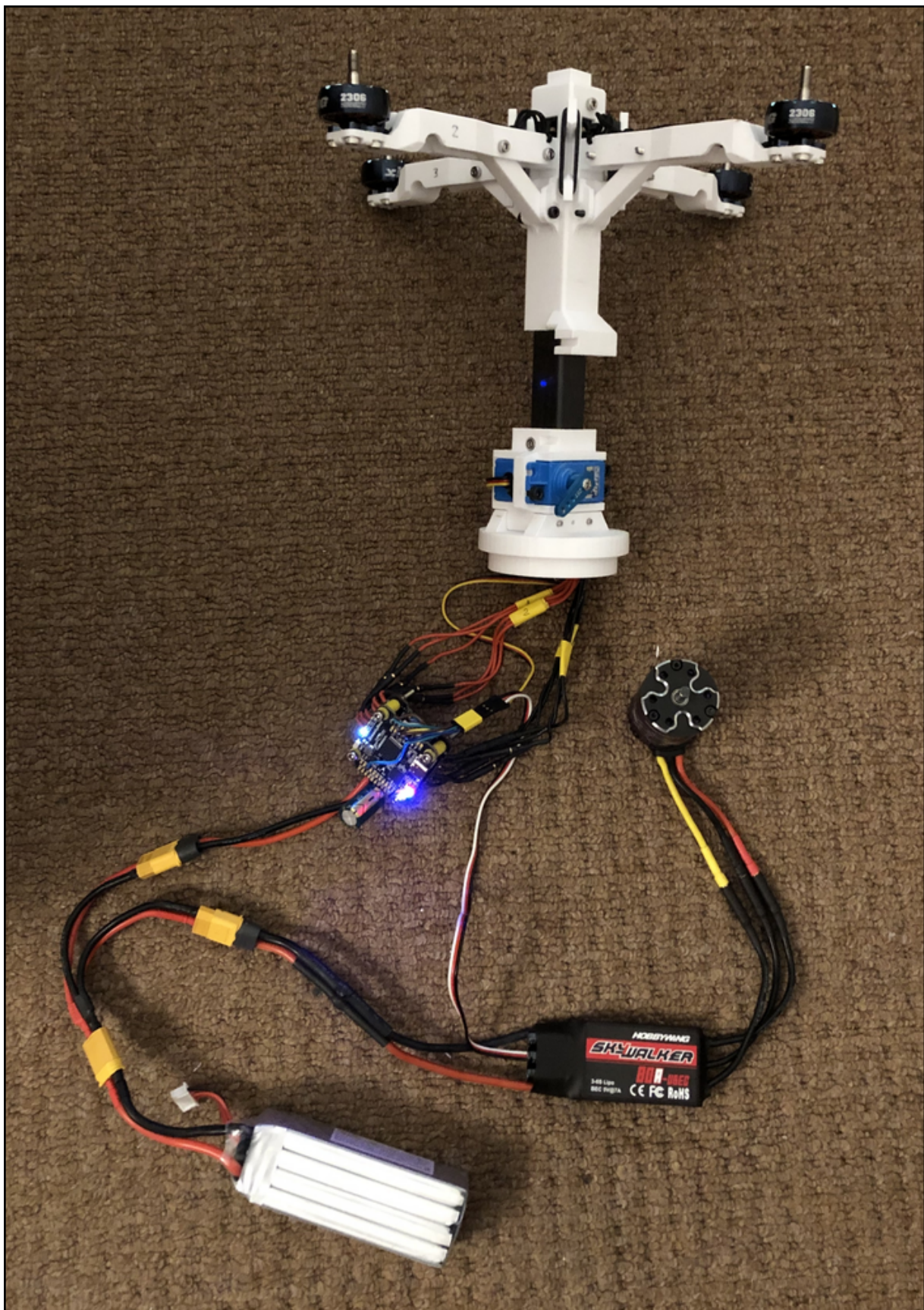


Figure I.3: Power distribution from battery to flight computer and motors

## Appendix J

### Wiring

Since the unfolding mechanism had so many moving parts, the wires could not be simply tied to the runners or central shaft as they would require a large amount of slack to account for their position change when the bottom runner moved up during unfolding. Having extensive slack in the wiring could result in the wires being wedged between the two runners. Instead, the motor wiring was secured with cable ties to the frame arms and passed into the hollow central shaft through a hole in the top runner. This resulted in a very small and controlled amount of slack in the wiring, which was not an issue (see **Figure J.1**). The wiring ran along the hollow shaft to the bottom (see **Figure J.2**) where a cutout was made for the wires to exit into a wire hole in the waterproof compartment which would later be sealed with silicone sealant (see **Figure J.3** and **Figure 5.2**). Bullet connectors were attached to the ends of the wire to allow for disconnecting the motors from the flight computer in case a 3D-printed part had to be remanufactured due to design iterations or an unexpected fracture.

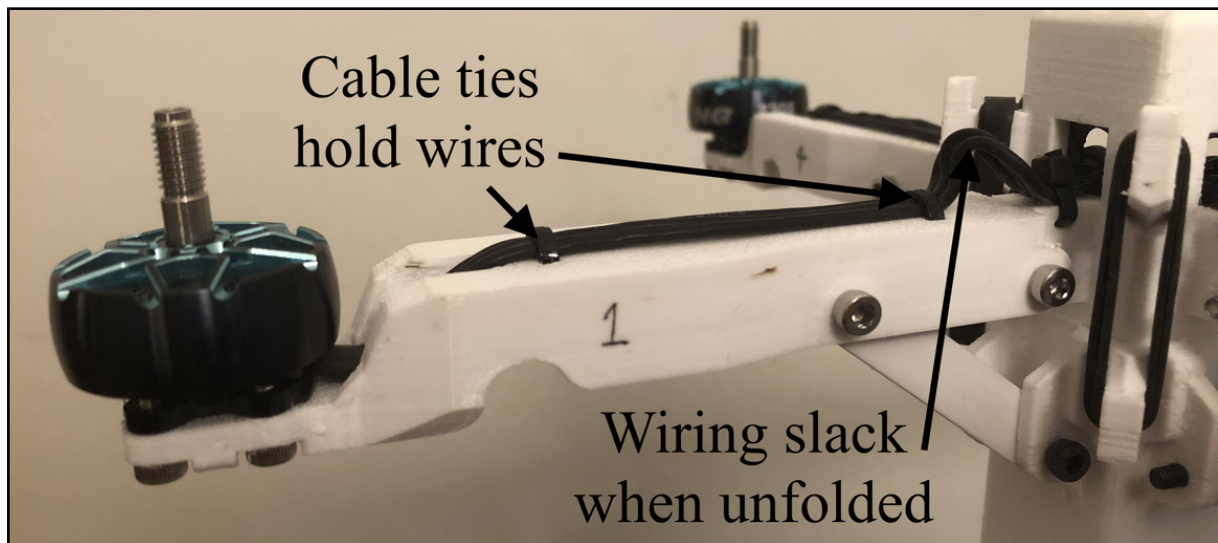


Figure J.1: Wiring from the aerial motors running along the frame arms into the hollow shaft

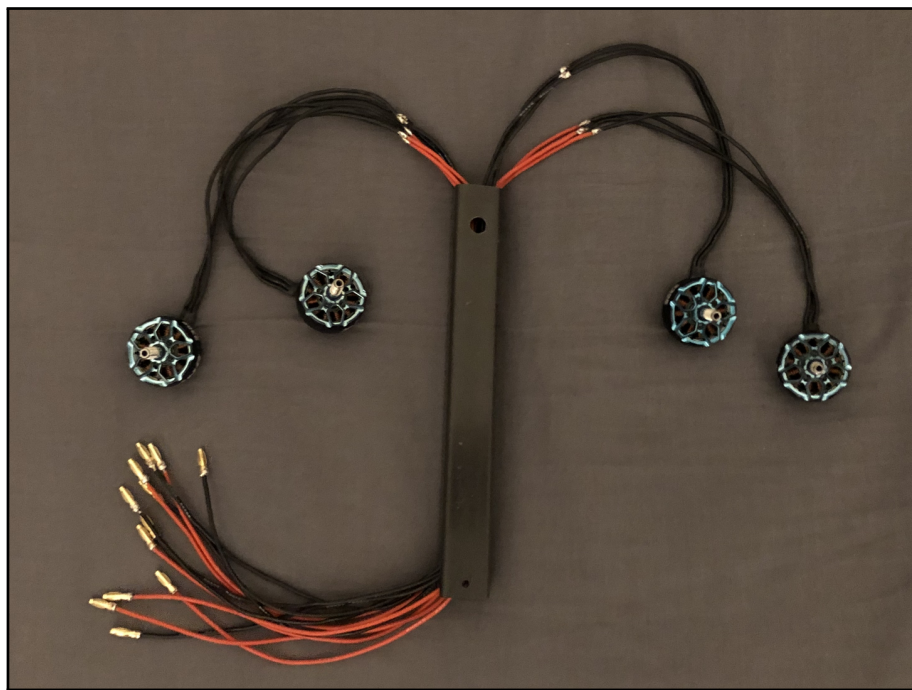


Figure J.2: Hollow shaft allows for motor wires with bullet connector ends to run down to the flight computer

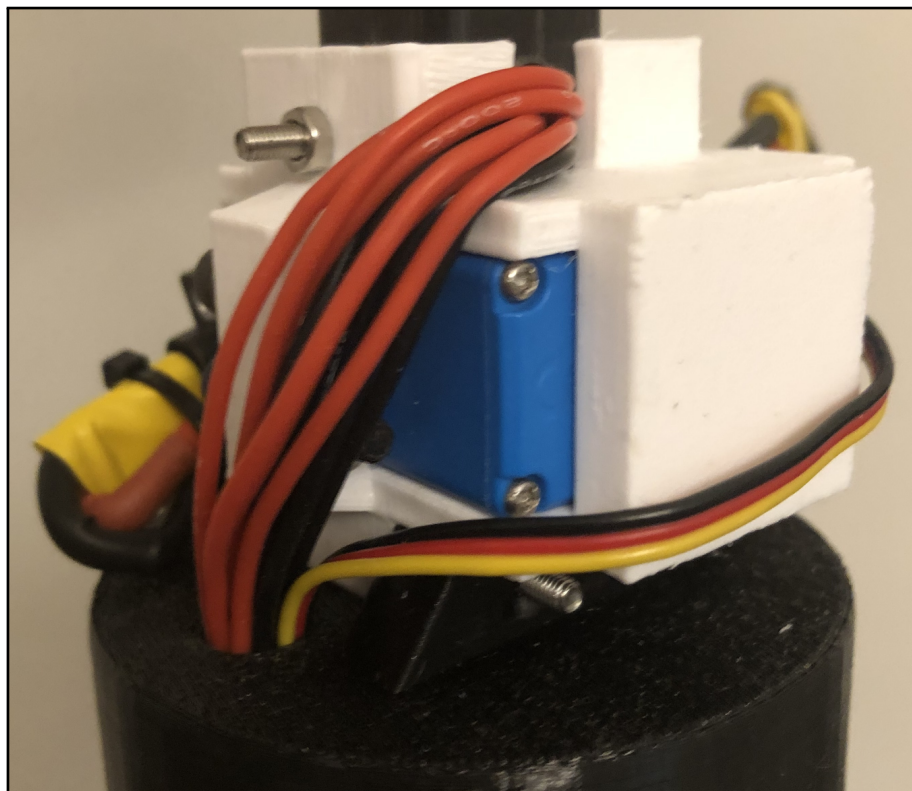


Figure J.3: Wiring running from the bottom hole of carbon fiber rod into the waterproof compartment

## Appendix K

### Radio and GPS

ExpressLRS is also popular in the custom quadcopter building community which meant that compatible receivers and transmitters were readily available. It uses the 2.4 GHz frequency band which is the same as Bluetooth, however, the purchased transmitter (see **Figure K.1**) is capable of achieving a range of up to 5 km (plenty for this use case).



Figure K.1: Jumper T Lite V2 Transmitter (ELRS)

Additionally, a magnetometer and GPS module (see **Figure K.2**) were connected to the flight computer to allow for accurate location and heading determination when above the water (required for the autonomous hover to maintain a fixed horizontal position).



Figure K.2: GPS module

## **Appendix L**

# **Additional Electronic Material**

- L.1 Aquatic Motor Running (link to video)**
- L.2 Aerial Motors Running (link to video)**
- L.3 Unfolding Mechanism Opening (link to video)**
- L.4 Slow Motion Experiment (link to video)**
- L.5 Associated CAD Files (link to drive)**
- L.6 Raw Experiment Tracking Data (link to drive)**